The Astrophysical Journal, 593:809–830, 2003 August 20

HUBBLE SPACE TELESCOPE OBSERVATIONS OF HIGH-VELOCITY Lyα AND Hα EMISSION FROM SUPERNOVA REMNANT 1987A: THE STRUCTURE AND DEVELOPMENT OF THE REVERSE SHOCK

Eli Michael,[1] Richard McCray,[1] Roger Chevalier,[2] Alexei V. Filippenko,[3] Peter Lundqvist,[4] Peter Challis,[5] Ben Sugerman,[6] Stephen Lawrence,[6] C. S. J. Pun,[7,8] Peter Garnavich,[9] Robert Kirshner,[5] Arlin Crotts,[6] Claes Fransson,[4] Weidong Li,[3] Nino Panagia,[10] Mark Phillips,[11] Brian Schmidt,[12] George Sonneborn,[7] Nicholas Suntzeff,[13] Lifan Wang,[14] and J. Craig Wheeler[15]

Received 2002 August 21; accepted 2003 May 4

ABSTRACT

We present two-dimensional line profiles of high-velocity ($\sim\pm$12,000 km s^{-1}) Lyα and Hα emission from supernova remnant 1987A obtained with the Space Telescope Imaging Spectrograph between 1997 September and 2001 September (days 3869–5327 after the explosion). This emission comes from hydrogen in the debris that is excited and ionized as it passes through the remnant's reverse shock. We use these profiles to measure the geometry and development of the reverse-shock surface. The observed emission is confined within $\sim\pm30^{\circ}$ about the remnant's equatorial plane. At the equator, the reverse shock has a radius of $\sim$75% of the distance to the equatorial ring. We detect marginal differences (6% $\pm$ 3%) between the location of the reverse-shock front in the northeast and southwest parts of the remnant. The radius of the reverse shock surface increases for latitudes above the equator, a geometry consistent with a model in which the supernova debris expands into a bipolar nebula. Assuming that the outer supernova debris has a power-law density distribution, we can infer from the reverse-shock emission light curve an expansion rate (in the northeast part of the remnant) of 3700 ± 900 km s^{-1}, consistent with the expansion velocities determined from observations in radio (Manchester et al.) and X-ray (Park et al.; Michael et al.) wavelengths. However, our most recent observation (at day 5327) suggests that the rate of increase of mass flux across the northeast sector of the reverse shock has accelerated, perhaps because of deceleration of the reverse shock caused by the arrival of a reflected shock created when the blast wave struck the inner ring. Resonant scattering within the supernova debris causes Lyα photons created at the reverse shock to be directed preferentially outward, resulting in a factor of $\sim$5 difference in the observed brightness of the reverse shock in Lyα between the near and far sides of the remnant. Accounting for this effect, we compare the observed reverse-shock Lyα and Hα fluxes to infer the amount of interstellar extinction by dust as $E(B-V) = 0.17 \pm 0.01$ mag. We also notice extinction by dust in the equatorial ring with $E(B-V) \approx 0.02$–0.08 mag, which implies dust-to-gas ratios similar to that of the LMC. Since Hα photons are optically thin to scattering, the observed asymmetry in brightness of Hα from the near and far sides of the remnant represents a real asymmetry in the mass flux through the reverse shock of $\sim$30%. We discuss future observational strategies that will permit us to further investigate the reverse-shock dynamics and resonant scattering of the Lyα line and to constrain better the extinction by dust within and in front of the remnant.

Subject headings: shock waves — supernovae: individual (SN 1987A) — supernova remnants

1. INTRODUCTION

As supernova (SN) 1987A's outer envelope expands into its surrounding circumstellar environment (Crotts, Kunkel, & Heathcote 1995; Plait et al. 1995; Burrows et al. 1995) a double-shock structure forms (Chevalier 1982), consisting of a forward shock (the blast wave) that propagates into the circumstellar gas, a reverse shock that propagates backward (in a Lagrangian sense) into the SN debris, and a contact discontinuity separating the shocked circumstellar material and shocked debris. Observations in different bands enable us to distinguish the emission from the parts of this double-shock structure. The rapidly brightening spots observed on the inner circumstellar ring (Lawrence et al. 2000a) are the

[1] JILA, University of Colorado, Campus Box 440, Boulder, CO 80309-0440; dick@jila.colorado.edu.
[2] Department of Astronomy, University of Virginia, P.O. Box 3818, Charlottesville, VA 22903-0818.
[3] Department of Astronomy, University of California, Berkeley, CA 94720-3411.
[4] SCFAB, Stockholm Observatory, Department of Astronomy, SE-10691 Stockholm, Sweden.
[5] Harvard-Smithsonian Center for Astrophysics, 60 Garden Street, Cambridge, MA 02138.
[6] Department of Physics and Astronomy, 151 Hofstra University, Hempstead, NY 11590.
[7] Laboratory for Astronomy and Space Physics, Code 681, NASA Goddard Space Flight Center, Greenbelt, MD 20771.
[8] Current address: Department of Physics, University of Hong Kong, Pokfulam Road, Hong Kong.
[9] Department of Physics, University of Notre Dame, 225 Nieuwland Science Hall, Notre Dame, IN 46556.
[10] STScI, 3700 San Martin Drive, Baltimore, MD 21218; on assignment from the Space Science Department of ESA.
[11] Carnegie Institution of Washington, Las Campanas Observatory, Casilla 601, Chile.
[12] Mount Stromlo and Siding Spring Observatories, Private Bag, Weston Creek P.O., ACT 2611, Australia.
[13] Cerro Tololo Inter-American Observatory, Casilla 603, La Serena, Chile.
[14] Institute for Nuclear and Particle Astrophysics, E. O. Lawrence Berkeley National Laboratory, Berkeley, CA 94720.
[15] Department of Astronomy, University of Texas, Austin, TX 78712.

TABLE 1
STIS G140L Observations

Designation	Date	Days since SN	Exposure Time (s)	Slit Width (arcsec)	Slit P.A (degrees east of north)	Slit Offset[a] (arcsec)
L1	1997 Sep 27	3869	11222	0.5	−147.4	0.11
L2	1999 Feb 27	4387	14350	0.5	25.6	0.15
L3B	1999 Sep 28	4600	10478	0.2	−124.8	0.03
L3A	1999 Oct 7	4609	10478	0.2	−124.8	−0.24
L3D	1999 Oct 12	4615	10665	0.2	−124.8	0.43
L3C	1999 Oct 13	4616	10665	0.2	−124.8	0.19
L5	2001 Sep 24	5327	10700	0.5	−139.3	−0.12
H1	1997 Oct 6	3878	4795	0.2	−139.0	0.14
H2	1999 Feb 21	4381	10500	0.5	25.6	0.14
H3	1999 Sep 18	4590	7583	0.2	−149.0	−0.04
H4N	2000 Nov 3	5002	2476	2.0	−92.8	−0.92
H4S	2000 Nov 3	5002	2354	2.0	−92.8	0.86

[a] Perpendicular distance from SN centroid to slit center.

result of the impact of the blast wave with dense obstacles that protrude inward from the ring (Michael et al. 2000; Pun et al. 2002). The 0.5–8 keV X-ray emission observed from the remnant comes primarily from the hot shocked gas behind the blast wave (Burrows et al. 2000; Michael et al. 2002), while the radio emission (Manchester et al. 2002) traces relativistic electrons accelerated by the shocks and the turbulent magnetic field between these shocks.

Emission from the reverse shock appears as high-velocity ($v \approx \pm 12,000$ km s^{-1}) components seen in Lyα and Hα. This emission is caused by collisional excitation of neutral hydrogen atoms in the debris that cross the reverse shock. The presence of this emission was predicted by Borkowski, Blondin, & McCray (1997a) and observed in 1997 April by Sonneborn et al. (1998) with the Space Telescope Imaging Spectrograph (STIS) aboard the *Hubble Space Telescope* (*HST*). Michael et al. (1998a) showed how the reverse-shock geometry could be mapped through the two-dimensional line-profile shapes. In late 1997 and early 1998, the Supernova Intensive Study (SINS) collaboration obtained the Lyα and Hα line profiles through narrower slits and established the basic geometry of the reverse shock (Michael et al. 1998b). Michael et al. found that the reverse shock was located $\sim$75% of the distance to the inner ring, was brightest about the equatorial plane (within $\pm 30°$), and had a brightness distribution that departed from cylindrical symmetry. Here we continue and expand our analysis of the reverse-shock emission with STIS observations of the line profiles with better spatial coverage over multiple epochs.

In § 2 we present the observations and describe our procedure for registering the spectra to the SN centroid. In § 3 we describe the mechanism for hydrogen line emission at the reverse-shock surface and calculate the relevant excitation and ionization rates. In § 4 we show how the observed profiles can be used to map the reverse-shock emission. In § 5 we describe the time dependence of the reverse-shock geometry and analyze its light curve. We also discuss extinction toward and internal to the remnant and describe the effects of Lyα resonant scattering. In § 6 we discuss the Hα and Lyα emission coming from the interior of the remnant. We conclude in § 7 with a discussion of what these observations of the reverse shock tell us about the hydrodynamics of the young supernova remnant (SNR) and present a strategy to guide future observations.

2. OBSERVATIONS AND DATA REDUCTION

Table 1 lists observations of high-velocity Lyα and Hα emission from SNR 1987A that were obtained in several epochs from 1997 September 27 to 2001 September 24 (days 3869–5327 after the explosion) using the STIS G140L and G750L gratings. The labels indicate the observed line and epoch (and slit position in some cases); e.g., L3A stands for the Lyα profile obtained in the third observation epoch with slit position A.

Figure 1 displays the slit orientations on the equatorial ring for all of the observations. We chose the orientation and slit width for many of these observations so that spot 1 on the ring (Pun et al. 2002) was in the slit. Because of this constraint, most of the observations have the slit aligned northeast-southwest. Observations L3A–L3D were planned specifically to map much of the reverse-shock surface in Lyα emission. For this set of observations, a narrow (0.″2) slit was placed at four locations across the remnant. Since it would have been prohibitive to map the entire remnant, we chose to concentrate on the east side, where the observed radio emission (Manchester et al. 2002) and the subsequently observed X-ray emission (Burrows et al. 2000; Park et al. 2002) was brightest. In epoch 2 we used the same slit size and position for both the G140L and G750L observations.

2.1. *STIS G140L Grating Spectra*

With the G140L grating we can measure the profile of high-velocity Lyα λ1215.67 emission at a spectral resolution of $\sim$300 km s^{-1}. For each observation, we took several (four or five) exposures centered at dithered positions 0.″5 apart along the slit. We reduced the two-dimensional spectra with standard calibration files, removed hot pixels, and combined the dithered exposures.

In Figure 2 we show the L3A spectrum in the vicinity of Lyα, along with an image of the ring and the slit position. This profile is representative of all the observed Lyα profiles. Lyα emission is evident in bright arcs extending to high velocity ($\sim\pm$12,000 km s^{-1}) as well as in diffuse emission interior to these arcs. The line profiles contain several sources of contamination, which are labeled in Figure 2. The bright vertical band of emission at zero velocity is due to geocoronal Lyα emission filling the slit. Low-velocity N v

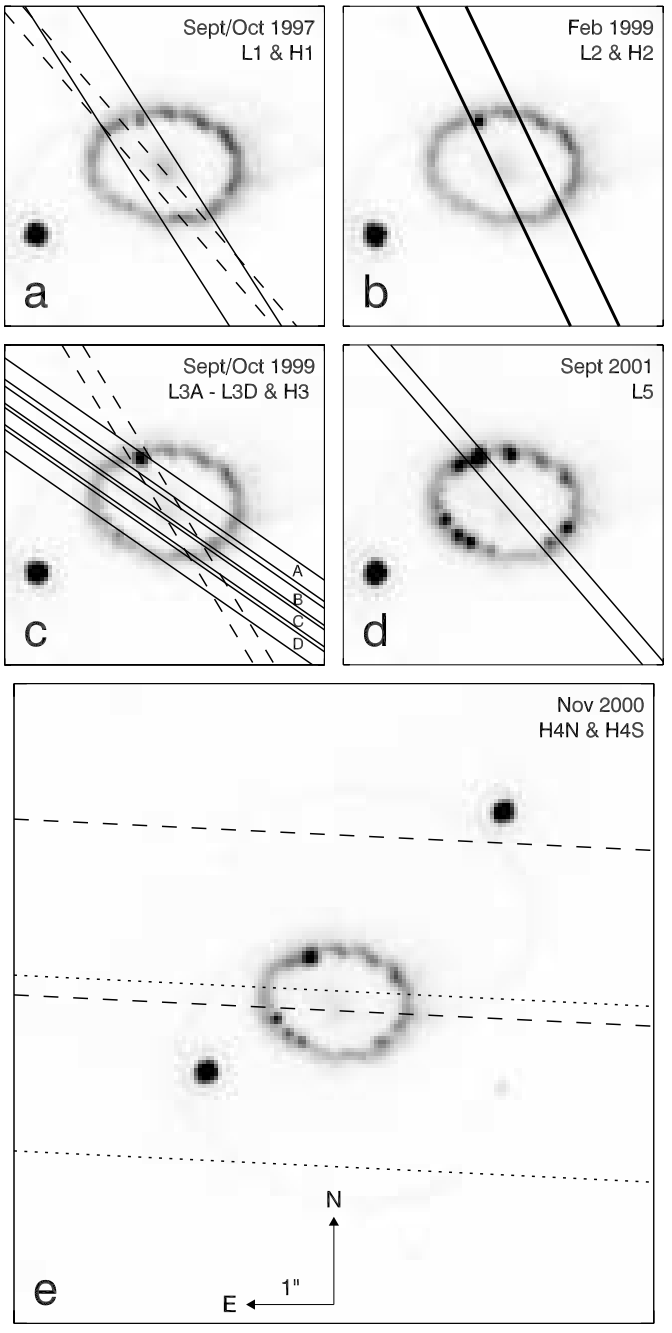

FIG. 1.—Slit positions on the equatorial ring for each of the different observation epochs (see Table 1 for designations): (*a*) L1 (*solid lines*) and H1 (*dashed lines*), (*b*) L2 and H2 (*thick solid lines*), (*c*) L3A–L3D (*solid lines*) and H3 (*dashed lines*), (*d*) L5, and (*e*) H4N (*dashed lines*) and H4S (*dotted lines*). The arrows in (*e*) are each 1″ in length. Note the brightening spots on the equatorial ring.

$\lambda\lambda$1239, 1243 emission from the ring system and the brightening spots contaminates the Lyα line profile at $v \approx 6000$ km s^{-1}. The velocity range of this contamination depends on which slit was used for the observation—$\Delta v \approx 2200(W_s/0\farcs2)$ km s^{-1}, where W_s is the width of the slit in arcseconds. Damping wings due to Lyα absorption by interstellar H I are apparent in the profile in the range $\sim\pm4000$ km s^{-1}. Interstellar absorption lines due to C I $\lambda\lambda$1191, 1259 and N I λ1199 are also apparent.

To isolate the high-velocity Lyα line profile we have removed these contaminants. The geocoronal emission has wings that extend beyond the slit and fainter contributions from lines other than Lyα. We remove it by subtracting an average geocoronal spectrum from regions above and below the source spectrum. Since the intrinsic distribution of N V $\lambda\lambda$1239, 1243 from the ring system is unknown, we mask out the regions of the profile that are contaminated by this emission. To remove the interstellar absorption lines, we construct composite absorption profiles by spatially integrating and combining the spectra from many separate observations. Since the emission from the remnant fills the slit (i.e., the source is not a point source), these measured profiles do not accurately represent the intrinsic absorption profiles. Therefore we constructed separate profiles for observations using the 0″.2 and 0″.5 slits.

TABLE 2
OBSERVED LYα FLUXES

Observation	Flux (10^{-14} ergs s^{-1} cm^{-2})
L1	6.54 ± 0.04
L2	7.83 ± 0.03
L3A	4.22 ± 0.02
L3B	3.56 ± 0.02
L3C	2.89 ± 0.02
L3D	2.07 ± 0.02
L5	5.85 ± 0.03

The extended nature of the source filling the slit is not an important consideration for the Lyα absorption since its damping wings are quite wide. To determine the interstellar H I absorption column, $N_{\rm H\,I}$, we assume that the majority of the absorbing gas lies in the LMC with a velocity of $\sim$300 km s^{-1}. By fitting the damping wings observed in a spatially integrated composite spectrum constructed from all of the observations made with the 0″.2 slit we find $N_{\rm H\,I} = (3 \pm 1) \times 10^{21}$ cm^{-2}. This result is consistent with the value $N_{\rm H\,I} = (4 \pm 1) \times 10^{21}$ cm^{-2}, found by fitting the absorption seen in the spectrum of the nearby star 2 (Scuderi et al. 1996), and also with a somewhat lower value, $N_{\rm H\,I} = (2.5 \pm 0.4) \times 10^{21}$ cm^{-2}, determined by Michael et al. (2002) through an analysis of the X-ray spectrum. We remove the Lyα absorption from the observed spectra assuming $N_{\rm H\,I} = 3 \times 10^{21}$ cm^{-2}. To avoid amplified noise, we mask out emission coming from velocities where the absorbed flux is less than 40% of the unabsorbed flux ($|v| \lesssim 3000$ km s^{-1}). The resulting "cleaned" line profile for the L3A observation is also shown in Figure 2.

Table 2 lists the observed fluxes in the Lyα line. To measure these fluxes we removed geocoronal emission and interpolated the Lyα profile underlying the N V $\lambda\lambda$1239, 1243 ring emission from nearby regions of the line profile. The tabulated fluxes do not include corrections for the interstellar line absorption discussed above. Since the observations are made through slits covering different portions of the remnant, a light curve made from the values tabulated in Table 2 would not be very meaningful. However, we do present a normalized light curve of the reverse-shock emission in § 5.4.

2.2. *STIS G750L Grating Spectra*

With the G750L grating we obtain the profile of high-velocity Hα λ6562.8 emission at a spectral resolution of $\sim$450 km s^{-1}. For each observation, we took multiple (two–eight) exposures centered at dithered positions 0″.5 apart

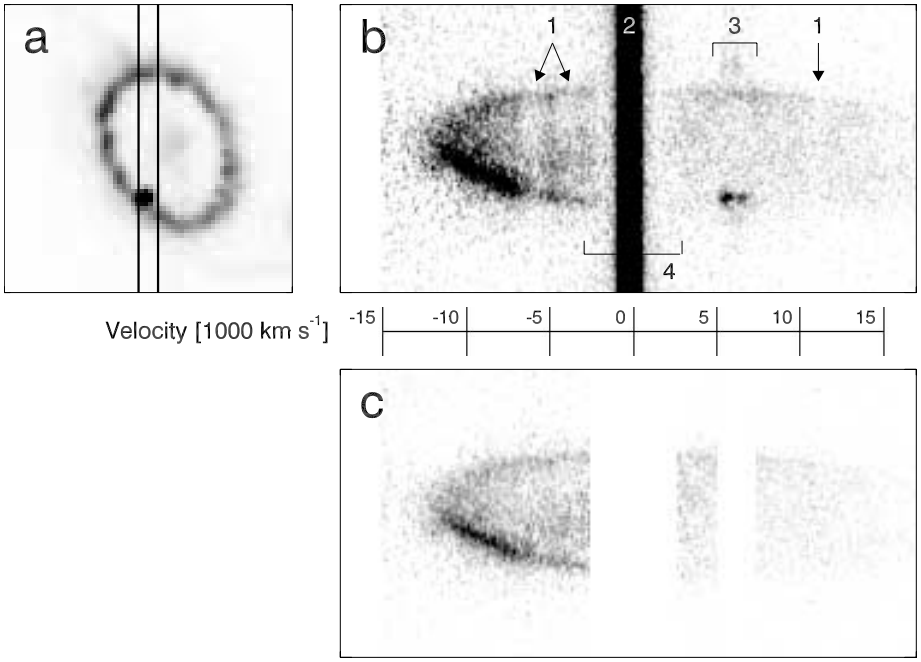

FIG. 2.—Typical Lyα line profile obtained with the STIS G140L grating. (*a*) Location of the 0.″2 slit used for this observation on the equatorial ring. The ring is shown at the same spatial scale as the line profile. (*b*) The spectrum in the vicinity of Lyα for the L3A observation. The dispersion direction is horizontal and the spatial direction is vertical. The velocity scale is relative to the systemic velocity of SNR 1987A, $v_{87A} = 287$ km s^{-1} (Meaburn et al. 1995). High-velocity Lyα from the remnant appears as bright arcs and emission interior to these arcs. Numbers label the various sources of contamination of the Lyα profile: (1) interstellar line absorption, (2) geocoronal Lyα emission filling the slit, (3) N v $\lambda\lambda$1239, 1243 emission from the ring system and spot (there are two N v spots since the line is a doublet), and (4) broad damping wings from interstellar H I absorption. (*c*) The "cleaned" Lyα profile after the contaminants have been removed or masked out. The images in (*b*) and (*c*) are shown at different intensity stretches.

along the slit. We reduced the two-dimensional spectra with standard calibration files and removed hot pixels and cosmic rays as we combined the dithered exposures. Figures 3 and 4 show two G750L spectra (of H3 and H4S) in the vicinity of Hα. Each spectrum is accompanied by an image of the ring and slit position.

In the H3 observation, high-velocity Hα emission is seen as arcs extending to $\sim\pm$12,000 km s^{-1}. In the H4S

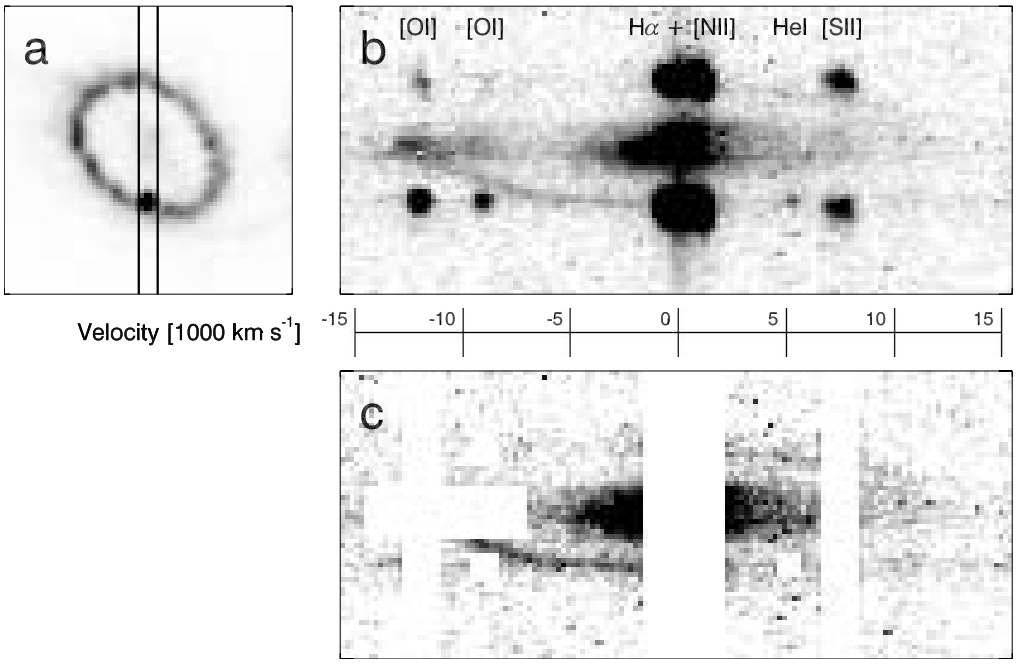

FIG. 3.—Hα line profile obtained with the STIS G750L grating. (*a*) Location of the 0.″2 slit used for the observation shown in (*b*). (*b*) The spectrum in the vicinity of Hα for the H3 observation. The dispersion direction is horizontal, and the spatial direction is vertical. The velocity scale is relative to the systemic velocity of SNR 1987A, $v_{87A} = 287$ km s^{-1} (Meaburn et al. 1995). The intensity is stretched to display the high-velocity Hα emission and results in other components of the spectrum appearing saturated. Emission lines from the equatorial ring and spot 1 are labeled. (*c*) The "cleaned" Hα profile after contaminants have been removed.

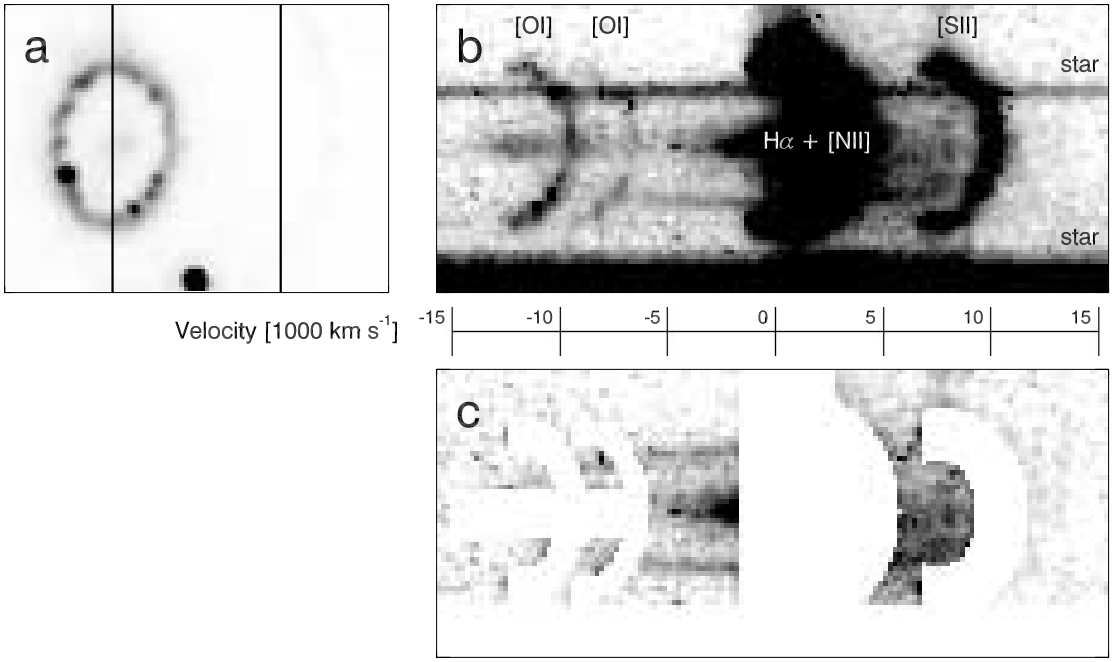

FIG. 4.—Hα line profile obtained with the STIS G750L grating. (*a*) Location of the 2″ slit used for the observation shown in (*b*). (*b*) The spectrum in the vicinity of Hα for the H4S observation. The dispersion direction is horizontal, and the spatial direction is vertical. The velocity scale is relative to the systemic velocity of SNR 1987A, $v_{87A} = 287$ km s^{-1} (Meaburn et al. 1995). The intensity is stretched to display the high-velocity Hα emission and results in other components of the spectrum appearing saturated. Emission lines from the equatorial ring are labeled. Emission from two stars are also present in the spectrum. (*c*) The "cleaned" Hα profile after contaminants have been removed.

observation the emission is also concentrated in arcs that extend to the blue side of the line, but the emission on the red side is more diffuse. The H3 and H4S profiles differ because different parts of the reverse shock surface fell within the slits.

The G750L spectra also display low-velocity emission lines ([O I] λλ6300, 6364; [N II] λλ6548, 6584; Hα; and [S II] λλ6717, 6731) originating from the equatorial ring. The ring emits in these lines because of delayed recombination and thermal emission from ions created by the initial SN flash (Lundqvist & Fransson 1996). Emission from the shock-excited hot spots on the ring is also visible in these lines (as well as in He I λ6678). The medium-velocity ($\sim\pm3000$ km s^{-1}) horizontal band of emission centered around zero velocity is Hα emission from the inner radioactive debris. Extended emission from the inner debris is also apparent at [O I] λλ6300, 6364. The spectra of two stars are also evident in the H4S observation.

For all observations we masked out the line emission from the ring, hot spots, and [O I] λλ6300, 6364 emission from the central debris. Two observations (H2 and H4S) contained overlapping emission from stars, which we removed by fitting the stellar profiles and interpolating their spectral slopes. We also removed faint continuum emission from the spots using the same technique. For the observations using the 2″ slit (H4S and H4N) we subtracted the diffuse LMC Hα emission that filled the slit. Figures 3 and 4 also show the "cleaned" Hα profiles for the H3 and H4S observations.

The Hα line profiles are too contaminated to extract precise measurements of the observed reverse-shock Hα flux for each epoch. Instead we estimate from the H4N and H4S profiles that the total observed Hα flux from the entire reverse shock is $\approx 5 \times 10^{-14}$ ergs s^{-1} cm^{-2}. To make this estimate we have masked out regions of these profiles that are contaminated by the ring lines and interpolated the Hα flux through these masked out regions. In addition, we remove the interior component of Hα emission (see § 6), which is not produced at the reverse shock.

2.3. *WFPC2 Imaging*

We use Wide Field Planetary Camera 2 (WFPC2) images of the ring and spots to register the location of the SN in our observations of the line profiles (§ 2.4). The SINS collaboration has been monitoring the remnant with WFPC2 imaging in several filters since 1994 with a cadence of ~0.5 yr. Table 3 lists the set of WFPC2 observations used in this paper. In order to maintain a reference frame consistent with the work of Sugerman et al. (2002), who measured the locations and proper motions of the spots on the equatorial ring, we use the WFPC2 images that were processed for their work. This processing includes the removal of cosmic rays and aberrant pixels and a correction for geometric distortions of the PC chip. As described by Sugerman et al. (2002), all of the images were geometrically registered using common stars with errors $\lesssim 0.05$ pixels. Stars 2 and 3 were removed using Tiny Tim model point-spread functions (PSFs) in order to prevent their diffraction spikes from interfering with the emission from the remnant.

2.4. *The SN Centroid*

One of our goals is to measure the location of the reverse-shock surface as a function of position angle (P.A.), latitude about the equatorial plane (θ), and time. In order to determine accurately the location of the reverse shock, we must establish a consistent reference frame for all observations. First we must determine where the SN centroid is located

TABLE 3
WFPC2 Observations

Date	Days since SN	Filter	Exposure Time (s)	Role in Registration
1994 Feb 3.....	2537	F656N	2400	...
1997 Jul 10	3790	F656N	5600	L1 and H1
1999 Jan 7	4336	F656N	7200	L2 and H2
2000 Feb 2.....	4727	F656N	3200	L3A–L3D and H3
2000 Nov 14	5013	F656N	4800	H4N and H4S
2001 Dec 7.....	5401	F656N	4000	L5
1994 Sep 24	2770	F555W	600	Defines SN location

along the slit for each observation. Then we can measure all reverse-shock positions relative to this centroid, which we assume to be the center of the remnant.

We determine the location of the SN centroid from the 1994 F675W filter image, where emission from the SN is still centrally concentrated and symmetric. We use the F675W filter to be consistent with the work of Sugerman et al. (2002), but we note that the centroid in the 1994 F656N image is offset from the F675W centroid by $\sim$10 mas. We regard this difference as indicative of the accuracy with which the SN centroid can be determined. Since all the WFCP2 images have been registered to each other, the SN centroid is then defined for each image. To determine the SN location in the STIS spectra, we identify common features (stars, spots, and ring emission) contained in both the images and spectra. For each spectral observation we use the F656N filter image that was obtained most closely in time. This procedure minimizes the errors created by changing fluxes in the ring and spots.

All of the G750L spectra contain emission from stars and spots (except the H1 observation, which lacks emission from a spot). For each of these spectra we determine the vertical location of stars and spots with Gaussian fits. We fit both the spot and ring profile simultaneously. Then, with the F656N filter images rotated to the proper position angles, we measure the vertical offsets from the SN centroid to the same stars and spots to determine the SN's vertical position in the spectrum. We find very good agreement (differences of $\lesssim$15 mas) between the location of the SN determined individually from each star and spot.

Since only one of the G140L observations (L3A) contained emission from stars, we use the vertical position of the N v $\lambda\lambda$1239, 1243 spot to find the SN location. We determine this position from Gaussian fits to the N v $\lambda\lambda$1239, 1243 line's spatial profile. We include background components of N v $\lambda\lambda$1239, 1243 ring emission and high-velocity Lyα emission in the fits. It is possible that the N v $\lambda\lambda$1239, 1243 emission from the spots comes from a different location than the Hα emission. This is so because these lines have different production efficiencies as a function of shock velocity, and a distribution of shock velocities is clearly present in the spots (Pun et al. 2002). However, since the spatial profiles of emission from the spots are still nearly unresolved, we believe that any offset between the N v $\lambda\lambda$1239, 1243 and Hα emitting regions is likely to be small compared with our spatial resolution. We can confirm this procedure by comparing the center determined from the N v $\lambda\lambda$1239, 1243 line the L3A spectrum with that determined from the stars. The centroids determined by the two techniques differ by $\lesssim$15 mas.

Three of the G140L observations (L3B, L3C, and L3D) do not contain emission from a spot on the ring. For these cases we match the spatial distribution of He II λ1640 emission from the ring to the Hα emission from the ring in the WFPC2 images. In doing so we convolve the spectral image of the ring in He II λ1640 with the WFPC2 PSF and the WFPC2 ring image with the STIS far-ultraviolet PSF. This procedure is less accurate than using point sources, and less certain, because the distributions of He II λ1640 and Hα emission from the ring are likely different. However, when we apply this technique to the G140L observations that do contain spot emission, we find the technique can locate the SN centroid with an accuracy of $\lesssim$40 mas.

The offset along the dispersion direction of the slit from the center of the remnant is also important in determining the location of the reverse shock. To determine these offsets, we measure the observed central wavelength of the line emission from spot 1 (N v $\lambda\lambda$1239, 1243 for the G140L observations and [O I] λ6300 for the G750L observations). The difference between the observed and expected wavelengths (allowing for the 287 km s^{-1} systemic velocity of the remnant; Meaburn, Bryce, & Holloway 1995) then indicates the offset of the spot and, by comparison with the WFPC2 images, the offset of the SN centroid from the center of the slit. Errors in this process include a centroid shift of emission from the spots of order $\sim$50 km s^{-1} (Pun et al. 2002) and the absolute accuracy of the wavelength calibration ($\sim$50 km s^{-1}). Adding these errors in quadrature, we find that we can determine the slit offset with an accuracy of $\sim$15 mas. For the L3B, L3C, and L3D observation the offset is determined only to an accuracy of $\sim$40 mas since no spot emission was present.

Accounting for all errors in the process, we should be able to locate the SN in the spectra to an accuracy of $\sim$20 mas ($\sim$55 mas for the L3B, L3C, and L3D observations). With a radius of $\sim$600 mas for the reverse-shock emission, we can therefore meaningfully distinguish only differences $\gtrsim$3% in the reverse-shock location between observations.

3. EMISSION PHYSICS

The reverse shock in SNR 1987A is a nonradiative collisionless shock in which thermalization of the supersonic fluid's bulk motion is mediated by a turbulent magnetic field. In such a shock the discontinuous jump in fluid variables occurs on the scale of an ion gyroradius, which is several orders of magnitude smaller than the particle's mean free path for deflection by collisions. An ion crossing the shock will immediately isotropize its bulk motion by spiraling around magnetic field lines. However, a neutral hydrogen

atom crossing the shock is not deflected by the magnetic field and will continue to travel through the shocked plasma with its preshock velocity. It will do so until it is ionized by collisions with particles in the postshock plasma. The resulting proton is deflected by the magnetic field and joins the proton postshock velocity distribution.

Prior to ionization the hydrogen atom can be collisionally excited and emit photons with a Doppler shift representative of the atom's velocity vector. The hydrogen atoms in the debris are expanding freely with velocity given by the Hubble law, $\boldsymbol{v} = \boldsymbol{r}/t$, where t is the time since the SN explosion and $\boldsymbol{r}$ is the radial position from the SN of a parcel of gas. Since the outer debris has cooled to $\lesssim 500$ K (Wang et al. 1996; Kozma & Fransson 1998), the velocity distribution of hydrogen atoms crossing the reverse shock is that of a cold radial beam. Therefore the position and geometry of the reverse-shock surface, the mass flux through that surface, and the kinetics of postshock excitation and ionization determine the emitted line profiles and strengths.

The maximum observed Doppler shift of the hydrogen lines at $t \approx 12$ yr is $\sim$12,000 km s^{-1}. From this we estimate that the reverse shock is located at a radius of $\sim 4.5 \times 10^{17}$ cm. The density of the outer SN envelope is assumed to have a power-law profile

$$\rho = \rho_0 \left(\frac{t}{10 \text{ yr}} \right)^{-3} \left(\frac{v}{10^4 \text{ km s}^{-1}} \right)^{-n},$$

with n observed to be ~ 9 (Eastman & Kirshner 1989) and theoretical values of ρ_0 ranging from $\rho_0 = 120$ amu cm^{-3} (model 14E1 of Shigeyama & Nomoto 1990) to $\rho_0 = 360$ amu cm^{-3} (model 10H of Woosley 1988). Therefore we expect the density of the debris material crossing the reverse shock to be $\sim$40 amu cm^{-3}.

The remnant's shocks will have complicated dynamics as a result of interactions with density inhomogeneities in the circumstellar gas (Borkowski et al. 1997a, 1997b). However, as a first approximation, we might assume the self-similar solution given by Chevalier (1982; with uniform circumstellar gas and $n = 9$). This solution yields a reverse-shock surface with outward velocity $\sim$80% of the blast-wave velocity, which has been established to be in the range 3500–5200 km s^{-1} (Manchester et al. 2002; Park et al. 2002; Michael et al. 2002). With these estimates, the SN debris crosses the reverse shock with relative velocity $v_s \approx 9000$ km s^{-1}. The mean postshock temperature of the plasma is given by $T_s = 3\bar{m}v_s^2/16k$, where $\bar{m}$ is the mean mass per particle, v_s is the shock speed, and k is Boltzmann's constant. For the reverse shock, $T_s \approx 10^9$ K. However, we emphasize that the Hα and Lyα line profiles are determined by the expansion velocity of the cold hydrogen atoms in the unshocked debris, not by the shocked gas.

3.1. *Excitation and Ionization of Hydrogen*

The postshock electron temperature, T_e, can be orders of magnitude lower than the mean shock temperature since each species carries energy proportional to its mass through the shock front. The timescale for electron-ion temperature equilibration through Coulomb collisions in the shocked gas is quite long ($\sim 10^6$ yr). However, collisionless plasma processes may partially equilibrate the electron and ion temperatures at the shock front (Cargill & Papadopoulos 1988). Ghavamian et al. (2001) found that the amount of equilibration decreases with increasing shock strength, so we expect that equilibration at the reverse-shock front will be small: $\beta = T_{e0}/T_s < 0.1$. In fact, the excitation and ionization rates of hydrogen are relatively insensitive to β. Neutral hydrogen atoms in the debris stream freely across the shock front and encounter a hot plasma with a shifted Maxwellian velocity distribution. While part of the impact velocity in a collision is due to thermal motions in the plasma, a comparable fraction comes from the relative motion of the neutral hydrogen atoms, which is independent of β.

Using the cross sections of Janev & Drawin (1993), we have calculated collisional excitation and ionization rates for hydrogen in the postshock plasma. We include impacts with electrons, protons, and alpha particles with relative fractions $\chi_p = 1$, $\chi_a = 0.2$, and $\chi_e = \chi_p + 2\chi_a$. Since all particles have nearly the same relative velocities, the ionization and excitation rates for each species are comparable. We calculate these rates using a shifted Maxwellian distribution with thermal width given by the degree of temperature equilibration and a bulk shift given by $\frac{3}{4}v_s$.

To determine the Lyα and Hα emissivity of a hydrogen atom once it crosses the reverse shock, we explicitly follow excitations to individual nl levels (up to $n = 5$). Since not all cross sections to all nl levels for all colliding species are available, we assume that the relative excitation rates to the $2s$ and $2p$ levels are the same for alpha particles as those for electrons and that the relative excitation rates to the $3s$, $3p$, and $3d$ levels are the same for protons, alpha particles, and electrons. We also assumed that all excitations to $n = 4$ and 5 go only into the s, p, and d states with the relative rates given by the electron impact excitation rates to the $3s$, $3p$, and $3d$ levels. Given the primary excitation rates, we determine the line emissivities from the radiative cascade paths for hydrogen calculated from the radiative transition rates given in Wiese, Smith, & Glennon (1966). Since the decay rates are very fast compared with the collisional rates, we assume that all excitations and ionizations occur from the ground state.

With a Sobolev optical depth of $\tau \approx 1000$, the debris crossing the reverse shock is optically thick to Lyman lines. Therefore we assume that the Lyman lines are a closed pathway for radiative cascades (case B). The Lyα line is unique, however, since no other efficient decay pathways exist. A Lyα photon will scatter until it can escape the remnant either through a spatial or spectral random walk (see discussion in § 5.3). Collisions may transfer populations between the $2p$ and $2s$ states (Pengelly & Seaton 1964). However, this transfer rate, $nC_{2p-2s} \approx 10^{-3}$ s^{-1}, is very slow compared with the effective decay rate of the $2p$ state, $\sim A_{2s-2p}/\tau_{\text{Ly}\alpha} \sim 10^6$ s^{-1}. The transfer rate is also slow compared with the two-photon decay rate for the $2s$ state ($A_{2s-1s} = 8.2$ s^{-1}; Nussbaumer & Schmutz 1984). Therefore radiative cascades that terminate in the $2s$ state will not produce Lyα photons.

Figure 5 shows the ionization and line excitation rates as functions of shock velocity and temperature equilibration. Taking the ratio of total ionization rate to the rate of producing Lyα by collisional excitation, we find that $\sim$0.8–1.05 Lyα photons are produced per hydrogen atom crossing the reverse shock. The ratio of production rates of Hα and Lyα, Hα/Ly$\alpha \approx 0.21$, is nearly independent of shock velocity and degree of temperature equilibration. The total ionization rate and postshock density indicate that the ionization zone will have thickness $\sim 10^{14}$ cm, which is quite small compared with the radius of the remnant ($\sim 6 \times 10^{17}$ cm)

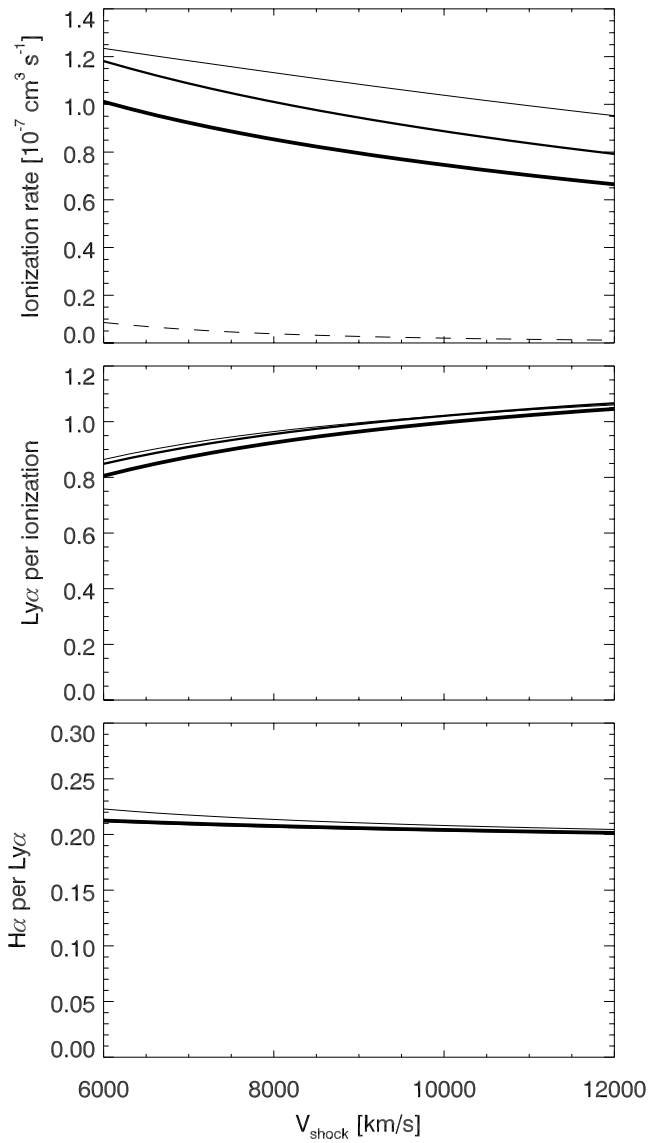

FIG. 5.—Ionization and excitation rates for hydrogen as functions of shock velocity and electron-ion temperature equilibration (β). Thin lines are for $\beta = 0$ (no equilibration), medium lines show $\beta = 0.01$, and thick lines show $\beta = 0.1$. *Top:* The total ionization rate (*solid lines*) due to collisions with electrons, protons, and alpha particles and charge transfer with protons and alpha particles. The proton-hydrogen charge transfer rate is also plotted (*dashed line*). Since the proton temperature is relatively insensitive to β, so too is the proton-hydrogen charge exchange rate. *Middle:* The number of Lyα photons produced per ionization for case B. *Bottom:* The number of Hα photons produced per Lyα photon for case B.

and the spatial resolution of *HST* ($\sim 6 \times 10^{16}$ cm for SNR 1987A).

In Figure 5 we also plot the rate of proton-hydrogen charge transfer. Since this rate is small compared with the total ionization rate, we expect a negligible amount of hydrogen line emission to be generated from the postshock proton velocity distribution. This situation differs from that in nonradiative shocks in other supernova remnants (Chevalier, Kirshner, & Raymond 1980) since the reverse shock in SNR 1987A is so fast. The charge transfer rates are sensitive to impact velocity and thus the shock velocity. Note that little hydrogen line emission will be produced by the blast wave since it is propagating into mostly ionized gas.

4. LINE PROFILE MAPPING

For homologously expanding supernova debris, the Doppler shift of a line photon will be proportional to its distance along the line of sight from the mid-plane. Therefore, surfaces of constant Doppler shift are planar sections through the debris and the observed line profiles can be used to map the depth of the emitting region in the debris. Figure 6 shows how emission from a cross section of the SN debris that is intercepted by a slit will be mapped onto the STIS detectors. A parcel of gas at a distance l along our line of sight from the SN mid-plane will have a line-of-sight velocity $v = l/t$, where $t = t_{\rm obs} - l/c$ accounts for photon time-of-flight delays across the remnant and $t_{\rm obs}$ is the observation time measured from the SN explosion. Each pixel in the detector records the flux from a volume element in the debris with size $\Delta V = \Delta s \Delta l \Delta w$, where Δs is the pixel's spatial size in the cross-dispersion direction, $\Delta l = t_{\rm obs}\Delta v/(1 + v/c)^2$ is the pixel's spatial size in the spectral direction, and Δw is the thickness of the cross section observed by the slit.

For infinitesimally thin slits, this mapping is unique since there are no parcels of gas with the same values of s and v. However, a slit's nonzero width blurs the mapping since two parcels of fluid on opposite sides of the slit having the same value of s but different line-of-sight velocities can be mapped to the same pixel in the spectrum. This blurring in velocity (or depth) increases with slit width.

Assuming that the line profiles are formed at the reverse-shock front, we create simulated line profiles to use in our analysis of the observed emission. Guided by the emissivity distribution in the observed profiles, we choose a model geometry for the emitting reverse-shock surface (e.g., a spherical shell). The line emissivity of the surface, ϵ, will be proportional to the mass flux, $\dot{m}$, through it. We assume, on the basis of the debris density distribution, that the mass flux is proportional to $t_{\rm obs}^5 r_{\rm rs}^{-8}$ (see § 5.4), where $r_{\rm rs}$ is the radius of the shock surface. We then disperse the line emission from each patch of the reverse-shock surface contained by the slit according to its location within the slit. The Doppler shift follows from the assumption of free expansion as noted above. Given the wavelength and flux from a piece of the shock surface, we multiply the emission by the spectrograph's throughput at that wavelength and place the resulting contribution to intensity at the appropriate position on the detector and with the appropriate point-spread function.

Alternatively, we can reverse the process shown in Figure 6 by assuming that all emission comes from the center of the slit. Then each pixel in the spectrum can be mapped to a unique location in the debris. Although the narrowest slit we have observed with is $\sim$15% of the remnant's size, maps constructed in this way still provide a useful way of interpreting the line profiles. In Figures 7–10 we show, for each observation, the line profile mapped into the ring coordinate system (where the equatorial plane is horizontal). For most observations emission (primarily blueshifted) from the northern parts of the remnant appears on the left-hand side of the image. Exceptions are the H4N and H4S observations, for which the left- and right-hand sides of the image show emission from the eastern and western parts of the remnant, respectively.

Figures 7–10 also show simulated maps made assuming that the reverse-shock emission comes from an equatorial

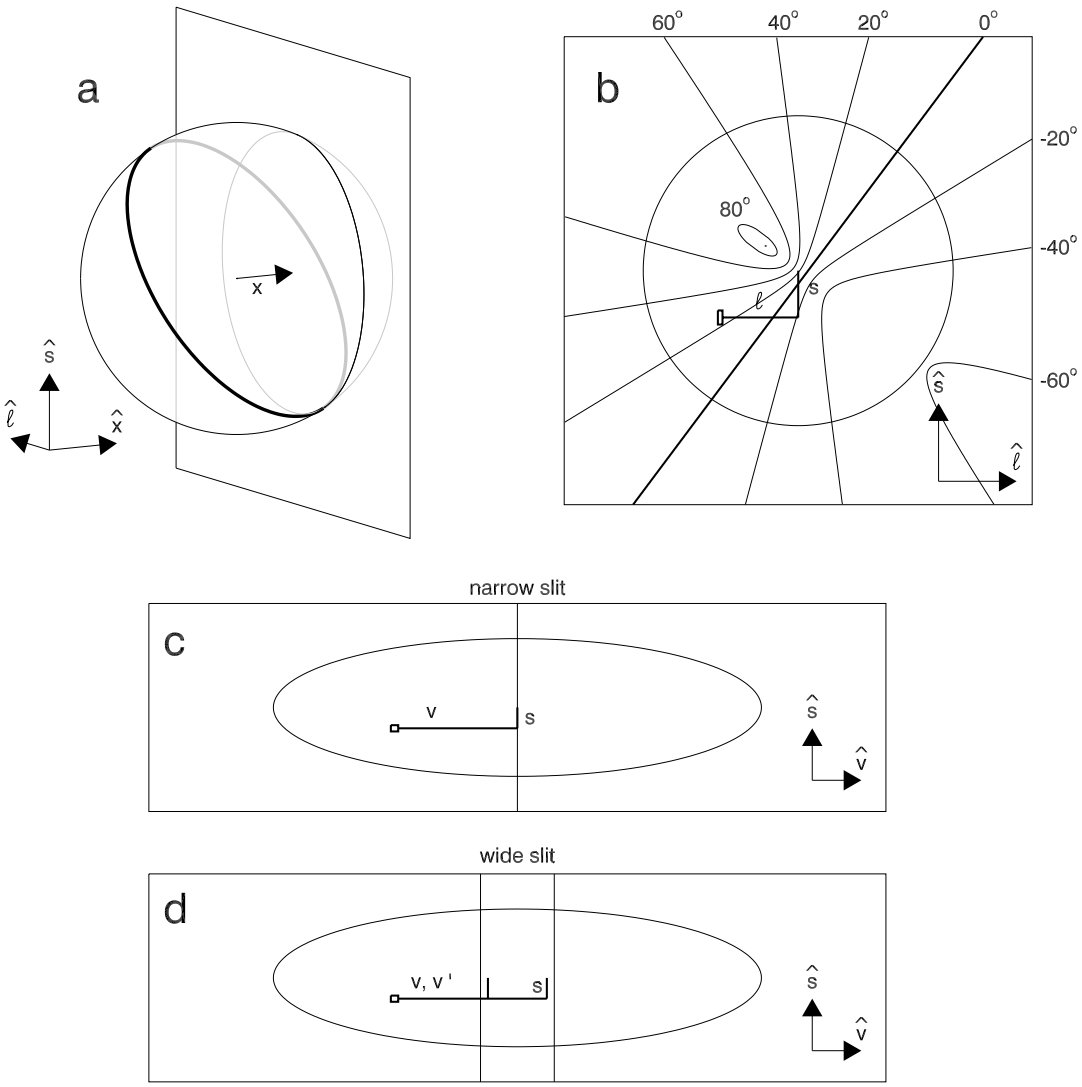

FIG. 6.—Demonstration of the mapping from physical to spectral space performed by the STIS spectrograph. (*a*) An infinitesimally thin slit (*shown as a plane*) intercepts a cross section of the SN debris (*represented as a sphere*). The ring plane is shown as a thick line on the equator of the sphere. Defining a coordinate system relative to the slit placement, $\hat{l}$ is the line-of-sight direction, $\hat{s}$ is the spatial direction along the slit, and $\hat{x}$ is the spatial direction perpendicular to the slit (x measures the slit offset from the debris center). (*b*) A side view of the intercepted debris cross section. Lines of constant latitude in the debris are shown at 20° intervals from the ring plane (*thick line*). These lines appear as conic sections since the slit is not centered on the SN. The plotted circle shows the radius of the inner surface of the equatorial ring. A parcel of fluid (*rectangle*) with coordinates (s, l) will be mapped to the spectrum (*c*) according to its position and Doppler shift, which is determined by $v = l/(t_{\rm obs} - l/c)$. (*c*) For narrow slits this mapping is unique, but (*d*) for wide slits this mapping become degenerate.

section (between ±30° latitude) of a thin spherical shell with radius 4.5×10^{17} cm. To match the observed profiles, we have also included a component of volumetric emission from the supernova debris interior to the reverse shock. For some of the observed maps we have stretched the intensity scale to highlight emission from the reverse shock. In some cases we have also stretched the intensity scale of the simulated maps so that the strength of the emission from the near (north) side of the remnant matches the observed strengths.

For these maps and simulations, we have assumed a distance to SNR 1987A of 50 kpc. A pixel's spatial size in the spectral direction is independent of distance, but the pixel size in the cross-dispersion direction decreases with the distance to the remnant. Therefore, the assumed distance influences the aspect ratio of the observed profiles (see Fig. 6*c*). We have normalized the emission in these maps to units of flux per unit volume, since each pixel along the line of sight observes a slightly different volume element (difference of 20% across the profile) due to time-of-flight delays across the remnant. We have also corrected these maps for differential extinction across the profiles by interstellar dust (see § 5.2).

Of these maps, the simplest to interpret are those representing the L3B and H3 observations, which were taken with narrow slits centered on the remnant. The basic shape of the reverse shock is readily apparent from these maps. The emission comes from a surface that can be represented approximately by a section of a sphere confined within ±40° of the equatorial plane and having radius about 75% of the distance to the ring. Emission from the near (north) side of the remnant appears substantially brighter than emission from the far side. This basic picture is confirmed in all the profiles.

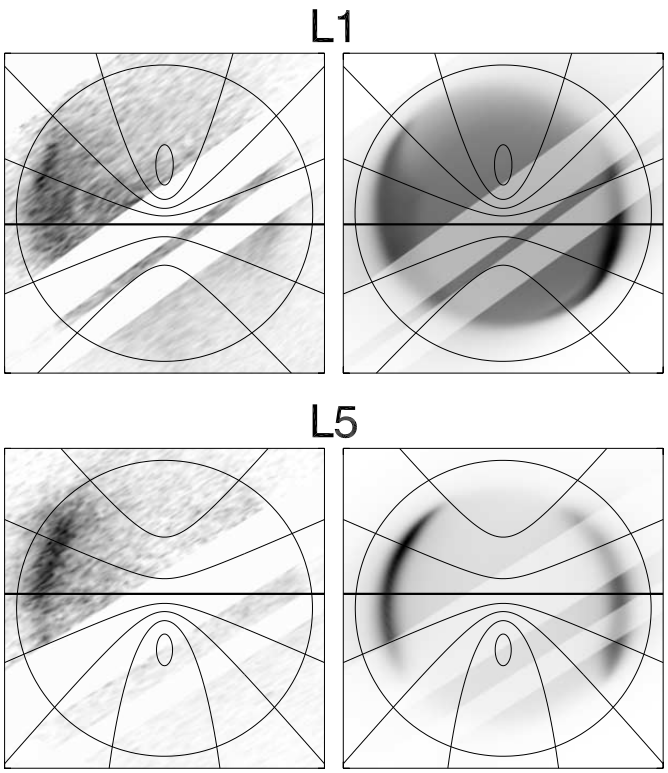

FIG. 7.—Cross-sectional emissivity maps for the L1 and L5 observations. The intersection of the slit with the equatorial (*ring*) plane is horizontal in these projections and is shown by the thick line. The top hemisphere of the remnant from our point of view is above this line. Lines of constant latitude spaced at 20° are shown as conic sections (see Fig. 6*b*). The radius of the circle is equal to that of the inner surface of the equatorial ring. Emission from the northern (near) side of the remnant appears on the left side of these images. The panels on the left are created from the observations assuming that all emission originates from the center of the slit. The panels on the right are emissivity maps created from simulated line profiles. To construct the simulated profiles we assume that the shock surface emits uniformly and has the shape of an equatorial section (±30° latitude) of a thin spherical shell with radius 4.5×10^{17} cm. We have also assumed a uniform component of interior emission for the Lyα profiles. Emission from where the observed maps are masked out has been made fainter in the simulated maps.

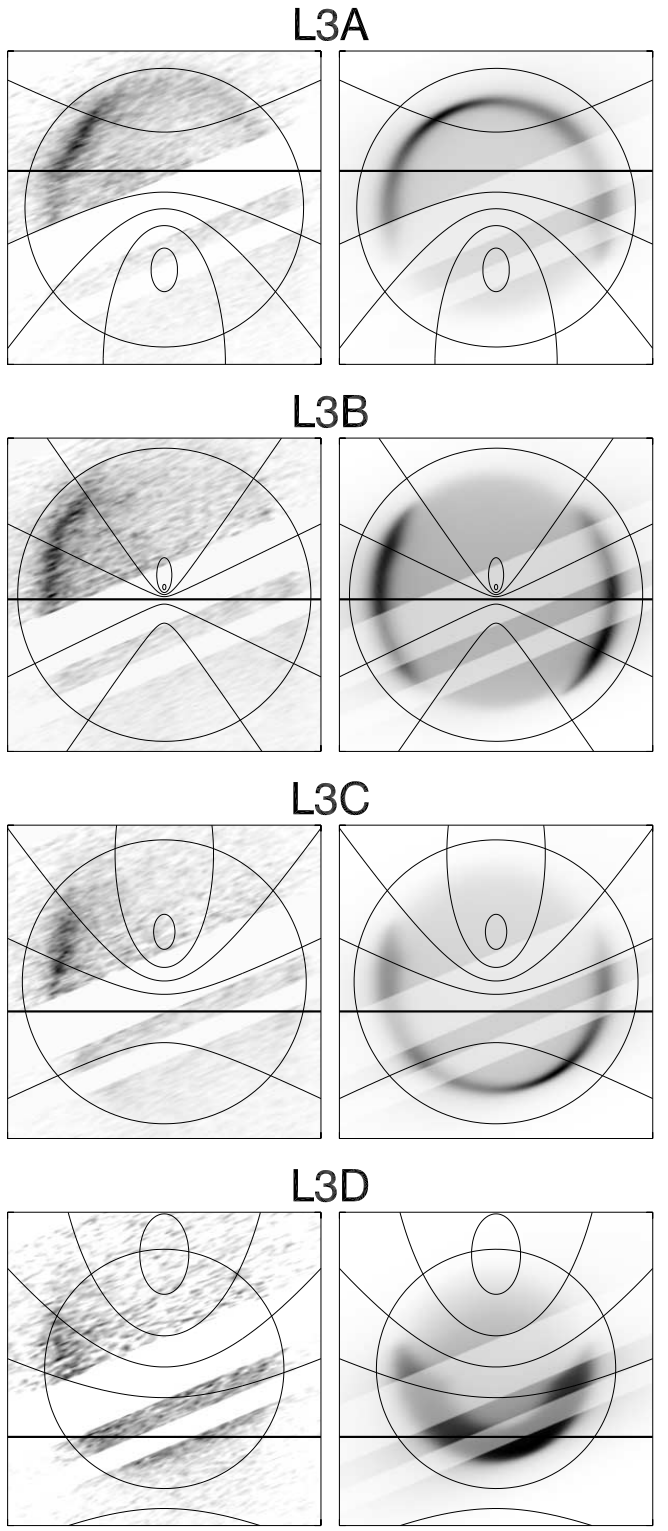

FIG. 8.—Cross-sectional emissivity maps for the L3A, L3B, L3C, and L3D observations. See Fig. 7 legend for details.

The shapes of the emitting surfaces in the observed and simulated maps correlate well. The most striking difference between them is the observed faintness of emission from the far side of the remnant compared with that from the near side. In §§ 5.2 and 5.3 we discuss possible interpretations of this asymmetry.

In observation L3D the emission from the reverse shock is extended in velocity since the reverse shock is primarily tangent to the slit plane. Therefore, emission from a substantial range of projected velocities is present in the profile. The H4N observation maps the north (near, blueshifted) half of the remnant and H4S observes the south (far, redshifted) half. For these maps we do not plot lines of constant latitude because the assumption that all emission comes from the center of the slit is poor for observations performed with the 2″ slit.

In Figure 10 we compare the epoch 2 Lyα and Hα profiles taken with the same slit positions. Since the emissivity ratio of Hα to Lyα is insensitive to the physical conditions of the shock, these line profiles should appear identical (except for small differences in the G140L and G750L PSFs). These profiles do appear similar but in fact they are not identical. We discuss the origin of these differences in §§ 5.2 and 5.3.

5. ANALYSIS

Figure 11 compares some observed emissivity distributions obtained from the maps presented in the previous

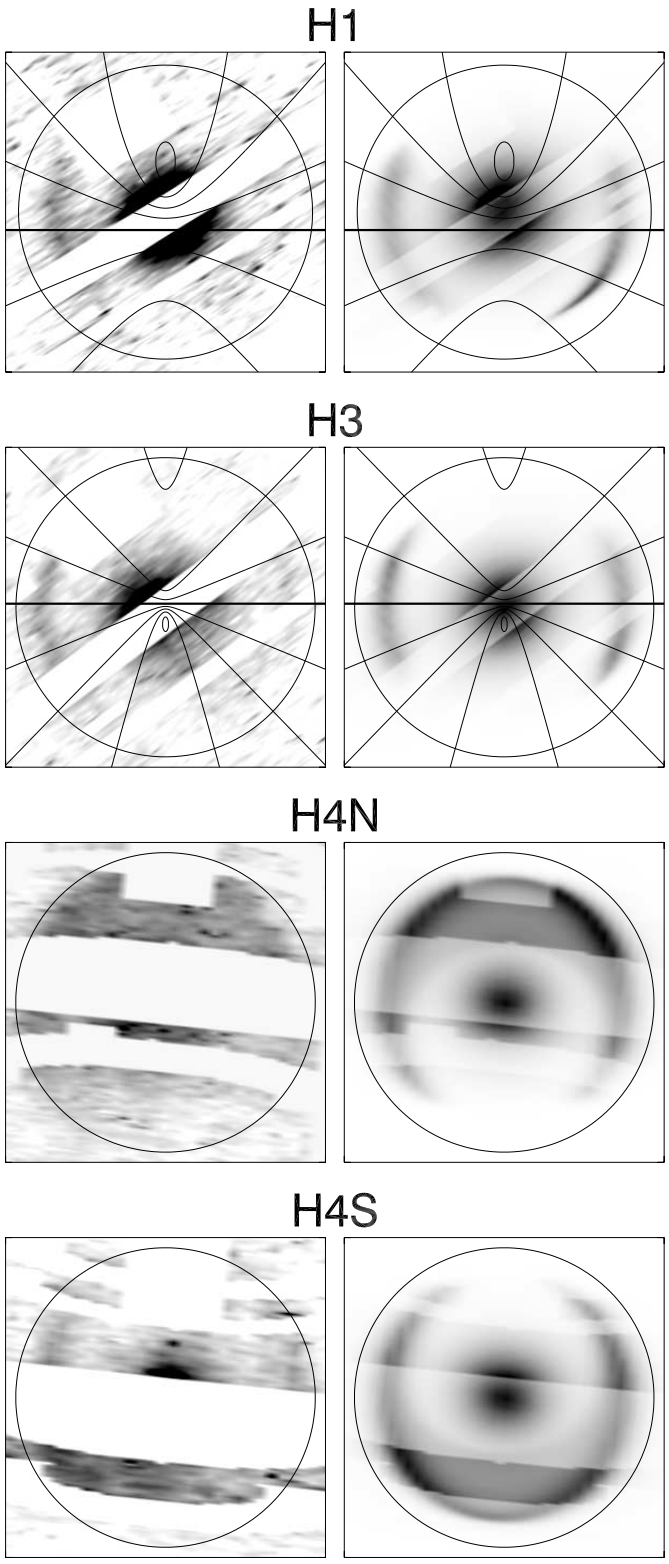

FIG. 9.—Cross-sectional emissivity maps for the H1, H3, H4N, and H4S observations. See Fig. 7 legend for details. For our simulations of the Hα profiles we have assumed that the Hα interior emission decreases exponentially with radius. Since the H4N and H4S observations were made with wide slits we do not show the lines of constant latitude for these maps.

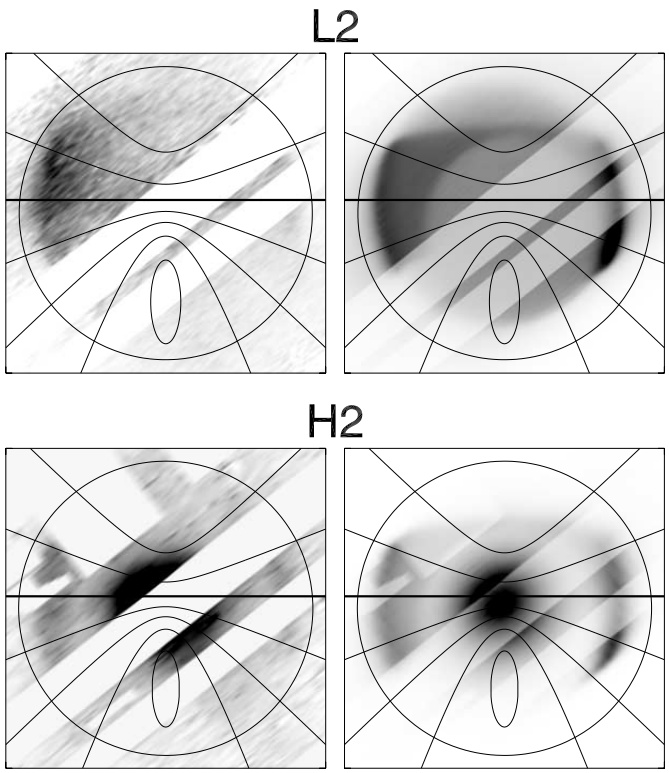

FIG. 10.—Cross-sectional emissivity maps for the L2 and H2 observations. See Figs. 7 and 9 legends for details. For this epoch the same slit size and position was used for both Lyα and Hα observations. Apart from slight differences in the G140L and G750L point spread functions, differences in these maps can be attributed mostly to differential extinction by the dust in the debris and ring system (see § 5.2).

section with their simulations. We plot the average emissivity as a function of radius integrated through latitudes 0°–20°. We include examples for Hα and Lyα from both the near and far sides of the remnant. In these distributions the reverse-shock emission creates the emission peak seen at $\sim 4.5 \times 10^{17}$ cm.

When observed with a slit with nonzero width, the line profiles are a convolution of velocity and spatial structure. Consequently, the observed emissivity maps and distributions do not precisely represent the actual emissivity of the remnant. Notice how the reverse-shock emission in the simulated maps shown in Figures 7–10 does not appear uniform with latitude, even though a uniformly emitting surface was assumed in the simulation. Therefore, we cannot accurately measure the reverse-shock location from, say, the observed peak of the emissivity distributions; nor can we use apertures to infer fluxes directly from the emissivity maps. Our ability to infer the true geometry and emissivity is further limited by the fact that most observations sampled slightly different regions of the remnant through different width slits at different angles and at different times.

In order to account for these effects, we use our simulated profiles to measure the position and emissivity of the reverse-shock surface independently of the parameters of the observation. First we create an average emissivity distribution from an observation for a desired section of the remnant. Then, adjusting the radius of the shock front, its emissivity, and the level of interior emission, we find a simulation that creates a closely matching distribution. We estimate errors for the position of the reverse shock from the range of simulated distributions that can reasonably match the observed one.

We must remove the interior emission component from the observed distributions to measure the flux from the

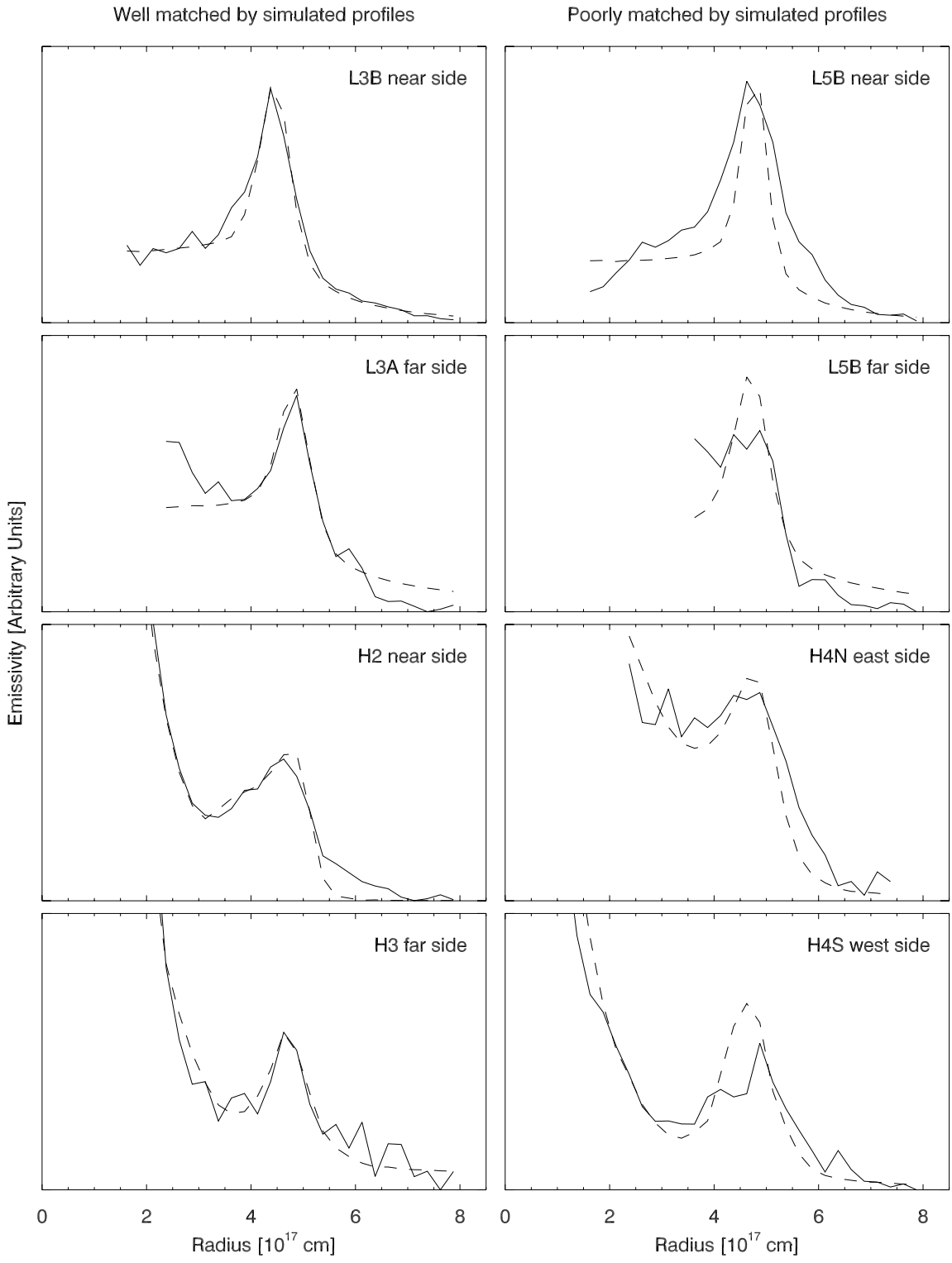

FIG. 11.—Emissivity as a function of radius averaged over 0°–20° latitude for several observations (*solid lines*) and their best matching simulations (*dashed lines*). The peaks in these distributions at a radius of $\sim 4.5 \times 10^{17}$ cm are due to emission from the reverse shock. The panels on the left show distributions that are well matched by simulations, while the panels on the right show profiles that are poorly matched.

reverse-shock surface. For the Lyα observations, we create a simulated distribution that contains only a uniform component of interior emission. For the Hα observations, we determine the interior emission from an exponential fit to the observed interior emission profile. We then measure the flux from the reverse shock by first subtracting the model interior emission profile from the observed distribution and integrating the remainder over the range of radius containing emission from the reverse shock. The error in the measured flux is due primarily to the uncertainty in the level of interior emission that we choose to subtract.

Finally, we compute a flux normalization factor for the distribution by integrating the simulated emission distribution created from a reference reverse-shock surface with uniform radius and emissivity. These normalization factors generally modify the measured fluxes by factors of $\lesssim 20\%$. Once all the fluxes have been normalized to those that would be produced by the reference geometry, the remaining differences in the fluxes are not sensitive to how the emission is dispersed in the line profile and can be attributed primarily to intrinsic differences in the emissivity of the reverse-shock surface.

In Figure 11 we illustrate extremes in the quality of the match between the observed and simulated distributions. In many cases the observed distributions are fitted quite well by their simulations (e.g., Fig. 11, *left-hand panels*). However, in some cases (e.g., Fig. 11, *right-hand panels*) one sees significant differences, such as those in the widths of the peaks. The emissivity distributions from the near side of the remnant are generally better matched to the simulations than the distributions from the far side of the remnant.

5.1. *Reverse-Shock Geometry*

5.1.1. *Equatorial Geometry*

In Table 4 we list the measured radii ($r_{\rm rs}$) and normalized surface emissivities ($\epsilon_{\rm rs}$) of the reverse shock on the equatorial plane. To avoid contaminants in the line profiles, and because emission from regions below the equator on the near side of the remnant are subject to absorption by the ring (§ 5.2), we have restricted these measurements to the emissivity distributions averaged over 0°–20° latitude. We define the longitude, ϕ, in the remnant as the angle measured in the ring plane from the nearest point on the ring to us (which lies at P.A. $\approx 9°$). For each observation the slit samples emission from the reverse shock over a range of longitudes, $(\phi - \Delta\phi/2)$ to $(\phi + \Delta\phi/2)$, depending on its width and location. The measured radii and emissivities are therefore average values over moderate ranges of latitude ($\Delta\theta \approx 20°$) and longitude ($\Delta\phi \approx 20°$–$60°$). The quoted errors for the reverse-shock location include measurement errors as well as errors in the registration of the SN centroid (§ 2.4). We have not included the L3D observation in this analysis since the observed profile is too diffuse, owing to the slit orientation used for this observation. The epoch 2 Hα and Lyα observations, which share the same slit size and position, give consistent results. In epochs in which we have overlapping longitudinal coverage the measured reverse-shock locations are consistent with each other within their uncertainties.

TABLE 4

Reverse-shock Radius and Surface Emissivity for Locations on the Equatorial Plane

Observation	ϕ (deg)	$\Delta\phi$ (deg)	$r_{\rm rs}$ (10^{17} cm)	Observed $\epsilon_{\rm rs}$[a]
L1	39	56	4.57 ± 0.15	1.00 ± 0.14
L1	204	60	4.49 ± 0.19	0.47 ± 0.07
L2	10	60	4.53 ± 0.16	1.77 ± 0.12
L2	229	56	4.79 ± 0.16	0.34 ± 0.05
L3A	13	34	4.63 ± 0.14	1.77 ± 0.09
L3A	276	30	4.87 ± 0.12	0.59 ± 0.05
L3B	51	26	4.49 ± 0.31	1.91 ± 0.13
L3B	241	24	4.76 ± 0.31	0.51 ± 0.05
L3C	72	26	4.42 ± 0.30	1.32 ± 0.07
L3C	222	22	5.06 ± 0.32	0.31 ± 0.05
L5	20	22	4.79 ± 0.27	4.28 ± 0.34
L5	240	24	4.76 ± 0.19	0.66 ± 0.12
H1	51	24	4.33 ± 0.19	1.08 ± 0.16
H2	40	58	4.57 ± 0.19	1.27 ± 0.18
H2	228	56	4.7 ± 0.25	0.86 ± 0.10
H3	22	22	4.63 ± 0.13	1.28 ± 0.13
H3	220	20	4.72 ± 0.15	0.99 ± 0.14
H4N	77	26	4.87 ± 0.21	2.22 ± 0.36
H4N	293	26	4.72 ± 0.13	1.49 ± 0.27
H4S	83	26	4.70 ± 0.13	1.96 ± 0.25
H4S	286	24	4.76 ± 0.17	1.57 ± 0.22

[a] Normalized to the L1 $\phi = 39°$ emissivity of 1.75×10^{10} photons s^{-1} cm^{-2}.

In Figure 12 we show the measured reverse-shock locations in the equatorial plane for the five different epochs. While the measured radii have substantial uncertainties, we can begin to see the global dynamics of the reverse shock. In the early epochs it appears that the reverse-shock front has traveled farther toward the southwest than it has toward the northeast, with differences in radius of $5\% \pm 4\%$ in epoch 2 and $7\% \pm 4\%$ in epoch 3. This trend is less apparent at later epochs.

The reverse-shock radius is increasing in time because of the global expansion of the remnant. In Figure 13 we plot the reverse-shock radius as a function of time for the northeast and southwest regions of the remnant. Assuming constant expansion, we find velocities of 2400 ± 1900 km s^{-1} in the northeast and 1800 ± 2100 km s^{-1} in the southwest. Unfortunately, these velocities are poorly constrained because of the limitations of our present astrometry; however, they are consistent with the more tightly constrained expansion rate determined from the reverse-shock light curve (§ 5.4).

5.1.2. *Latitude Dependence*

One of the most striking features of the emissivity maps shown in § 4 is that the reverse shock is brightest near the equatorial plane. A simple explanation is that the blast wave, encountering denser material near the equator, has not traveled as far as it has in the polar directions. The emissivity of the reverse-shock surface is proportional to the mass flux through it. As we shall see, at the equator the reverse shock has a smaller radius and hence reaches deeper into the denser debris. Therefore, we would naturally expect the reverse shock to be brighter at the equator than at higher latitudes. Since the density profile of the debris is very steep, modest differences in the location of the reverse shock will result in large differences in its emissivity.

Our observations allow us to investigate the latitudinal geometry of the reverse shock. Since the observed emission is sensitive to variable extinction in the remnant, we restrict our analysis to regions of the reverse shock located above the equator on the near side of the remnant. The latitudinal position of the reverse shock is best measured from the Lyα profiles from the L3A, L3B, and L5 observations, which were obtained with the 0.″2 slit. Figure 14 shows that the reverse shock is not spherical—it is elongated toward the poles with an ellipticity of $\approx 25\%$.

The observed flux from the reverse shock decreases very rapidly for latitudes $\gtrsim 40°$. If the reverse shock were a prolate ellipsoid with eccentricity 25%, we should have detected emission from these latitudes. The fact that we have not

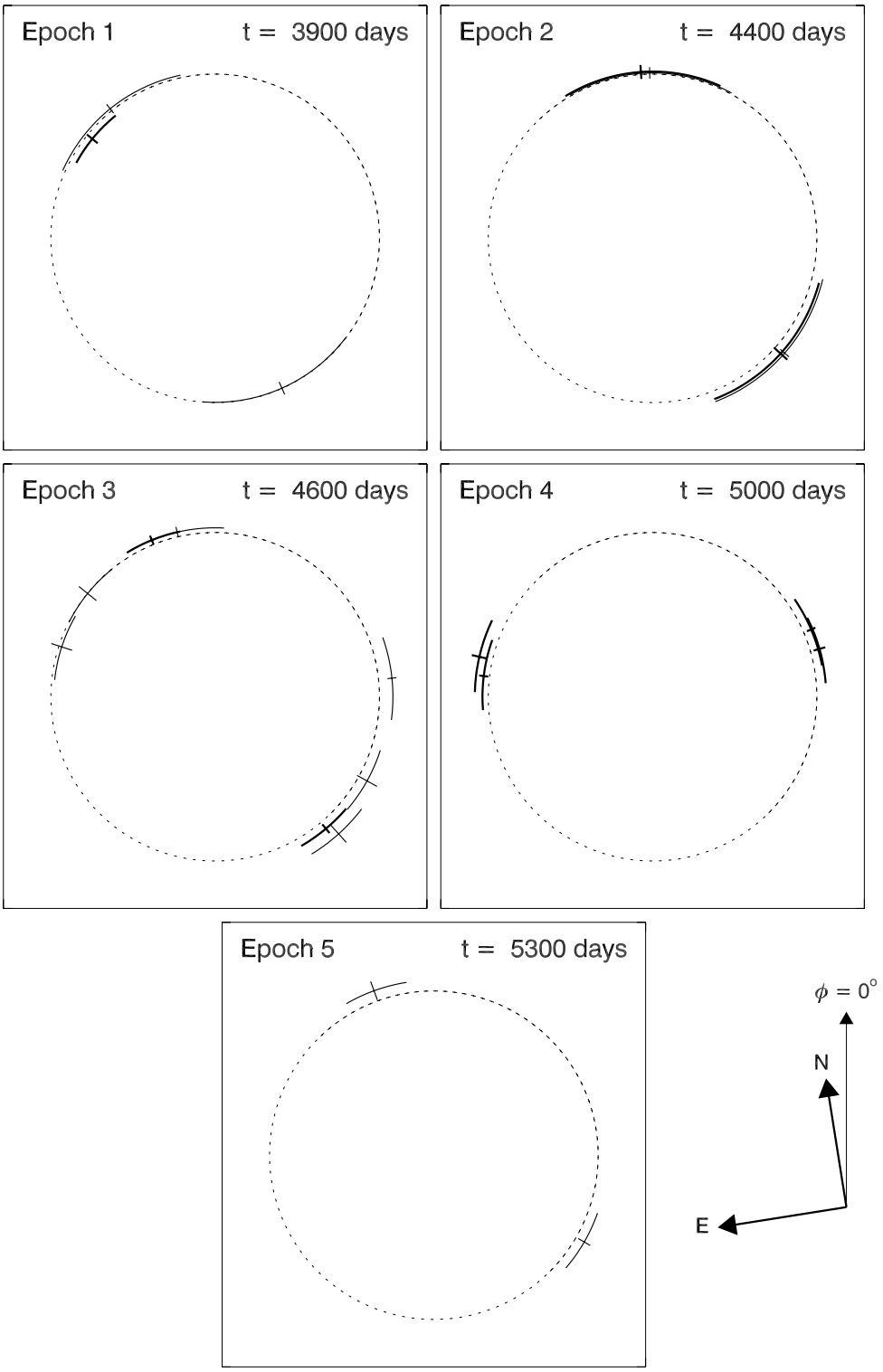

FIG. 12.—Measured locations of the reverse-shock surface in the equatorial plane for each observation epoch. Thin lines show measurements from the Lyα observations, and thick lines show the Hα measurements. The dotted line shows a reference radius of 4.5×10^{17} cm.

suggests that the density of the circumstellar matter decreases rapidly toward the poles, so that the blast wave and reverse shock have substantially greater radii in these directions and are much fainter than they would be for a prolate ellipsoid model.

The latitudinal geometry of the reverse shock is consistent with hydrodynamic models of the expansion of supernova debris into a bipolar nebula (Blondin, Lundqvist, & Chevalier 1996). It is beyond the scope of this paper to provide a detailed hydrodynamic model for the expansion of SNR 1987A into its circumstellar environment. However, we show in Figure 15 an idealized scenario that could account qualitatively for the observed geometry. It is a frame from a simulation, following Borkowski et al. (1997a), in which we

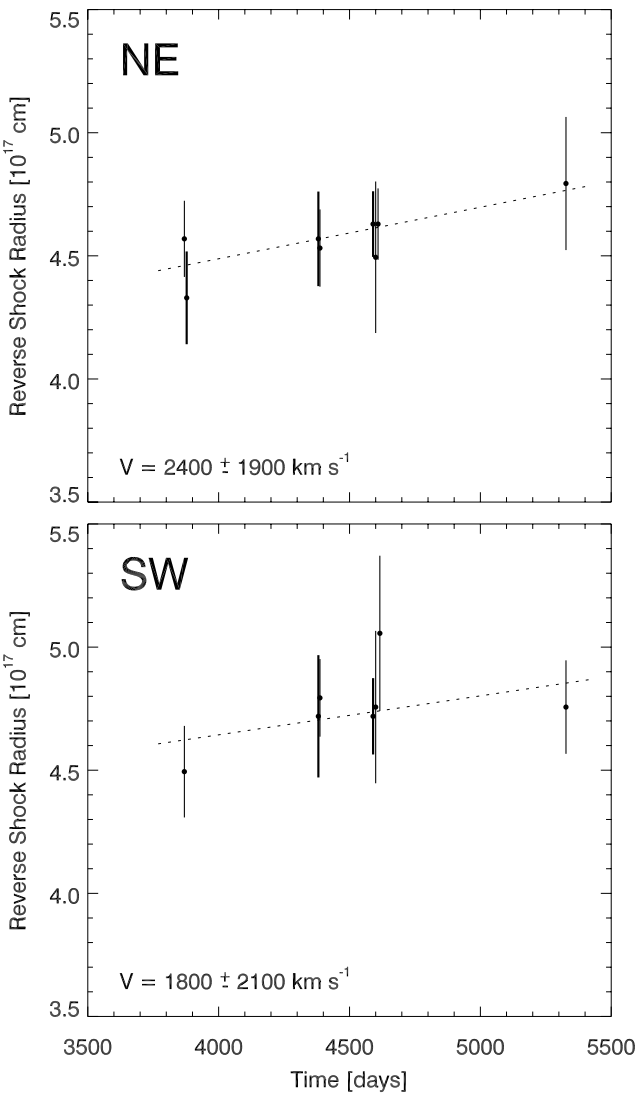

FIG. 13.—Reverse-shock positions on the equator as a function of time for the northeast and southwest regions of the remnant. Thin lines show measurements from the Lyα observations, thick lines show the Hα measurements. Dotted lines show fits for the reverse-shock expansion assuming a constant velocity v.

have assumed that the circumstellar gas consists of a toroidal H II region with major radius equal to the radius of the equatorial ring ($R_{\rm ring}$), minor radius equal to $R_{\rm ring}/2$, and density of 100 cm^{-3} embedded in a hot low-density (0.5 cm^{-3}) bubble caused by the shocked stellar wind of the blue-supergiant progenitor. The dense circumstellar gas in the equatorial plane confines the blast wave and reverse shock, while in the polar direction the shock structures have propagated much farther and the shocked gases have much lower density. This simulation resembles the observed structure of the reverse shock shown in Figure 14: the reverse-shock surface is confined to smaller radii for latitudes $\lesssim 40^\circ$, and its surface geometry in the equatorial region is not spherical but is elongated in the polar direction.

5.2. *Differential Extinction*

As we described in § 3.1, the photon emissivity ratio, Hα/Ly$\alpha \approx 0.21$, by a fast shock is nearly constant. But in SNR 1987A the observed ratios (Table 4) are in the range Hα/Ly$\alpha \approx 0.7$–3, much greater than the emitted ratio. This difference can be attributed largely, but not entirely, to extinction by interstellar dust.

The extinction by dust along the line of sight toward SNR 1987A has been measured from nearby stars to be $E(B-V) = 0.16 \pm 0.02$ mag (Fitzpatrick & Walborn 1990) and $E(B-V) = 0.19 \pm 0.03$ mag (Scuderi et al. 1996). The Galactic component accounts for $E(B-V) \approx 0.06$ mag, while the remaining extinction is caused by dust in the LMC.

We can compare the observed Hα/Lyα ratios with the expected emitted ratio to infer the interstellar extinction toward SNR 1987A. The epoch 2 observations, performed with the same slit size and position, are ideal for this purpose since we can compare the Hα and Lyα emission from the same regions of the reverse shock. While not observed with the same slit positions, Hα and Lyα emission from overlapping regions of the reverse shock were also obtained in epoch 3. To model the interstellar extinction, we assume a Galactic extinction law (Fitzpatrick 1999) with $E(B-V) = 0.06$ mag and calculate the LMC component using the observed emissivities and the extinction law of the 30 Doradus region (Fitzpatrick 1986).

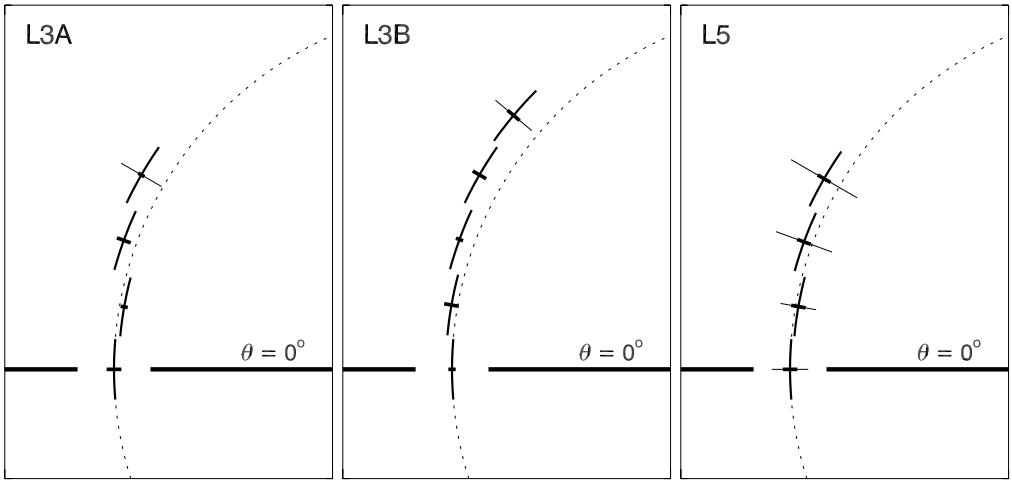

FIG. 14.—Reverse-shock positions for different latitudes (with 10° spacing) for emission from the near side of the remnant as measured from the L3A, L3B, and L5 observations. The thick horizontal lines show the equatorial plane ($\theta = 0^\circ$), and the dotted lines show circles with radii equal to the equatorial shock radius for each observation. Thick radial error bars indicate errors in the mean reverse-shock radius determined for the latitude section, and thin radial error bars show the range of reverse-shock radii implied by the width of the reverse-shock emissivity distributions.

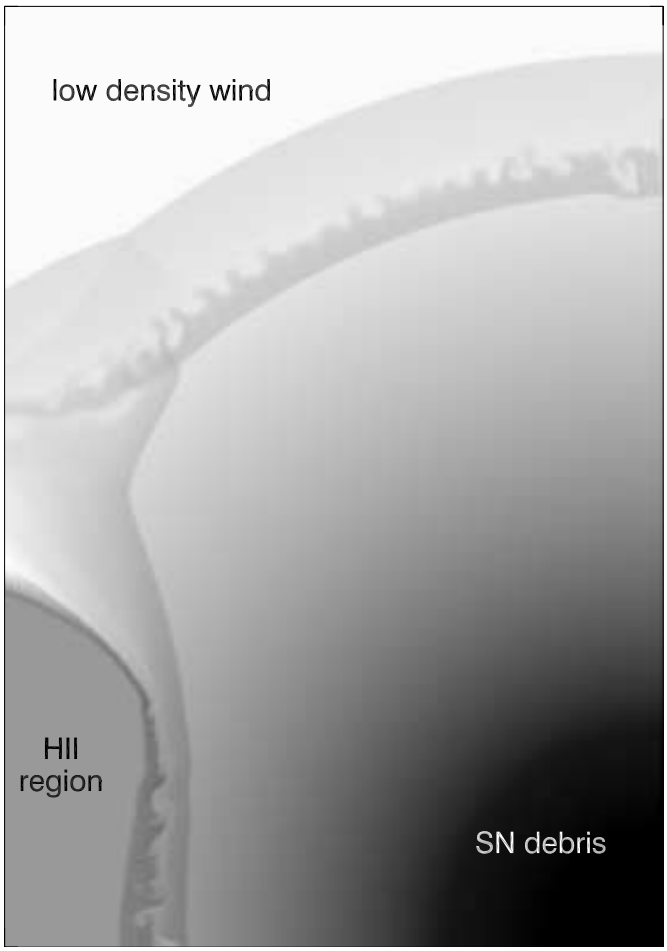

FIG. 15.—Frame from a hydrodynamic simulation of the interaction of the expanding SN debris with the circumstellar environment at $t = 13$ yr. The gray-scale image depicts density, with darker shades representing higher densities. The axis of symmetry for this simulation lies along the right edge of the image and the equatorial plane lies along the bottom edge.

The observed ratio Hα/Lyα in the reverse shock varies across the remnant. It has the lowest value, Hα/Lyα = 0.7 ± 0.1, for that part of the reverse shock that is nearest to the observer (emission on the left-hand side of the maps shown in Fig. 10). If we attribute this ratio entirely to interstellar dust, we infer an extinction $E(B-V) = 0.13 \pm 0.01$ mag, which is inconsistent with that determined by Fitzpatrick & Walborn (1990) and Scuderi et al. (1996) for the nearby stars. As we shall describe in the next section, this discrepancy is probably due to resonant scattering in the Lyα line.

The L3A and L5 line profiles (Figs. 7 and 8) show that the reverse shock on the near side of the remnant is substantially fainter at latitudes below the equator than it is above the equator. This asymmetry can be attributed to extinction by dust in the equatorial ring (see Fig. 16). Figure 17 shows the amount of additional reddening we measure for lines of sight through the ring. For epoch 2 we can use the observed Hα/Lyα ratio to determine the extinction. However, since we lack Hα observations corresponding to the L3A and L5 observations, we simply assume that the Lyα emissivity below the equator is equal to that measured for 0°–20° latitude to infer the extinction. Comparing the two techniques for the epoch 2 observations, we find this to be a reasonable assumption.

The amounts of reddening by the equatorial ring implied by this analysis range from $E(B-V) = 0.02$–0.08 mag, yielding dust-to-gas ratios in the ring comparable with the LMC ratio. The extinction by dust in the ring measured in epoch 2 appears lower than that implied by the other observations. This difference can be attributed to the fact that the epoch 2 observations were taken with wide (0.″5) slits, which allowed contamination of the line profiles by emission from regions of the reverse shock that are not blocked by the ring. None of the observations to date are ideal for measuring extinction by the ring. In § 7 we present an observational strategy that will improve these measurements.

The emission from the reverse shock on the far side of the debris (the right-hand side of the maps shown in Fig. 10) is

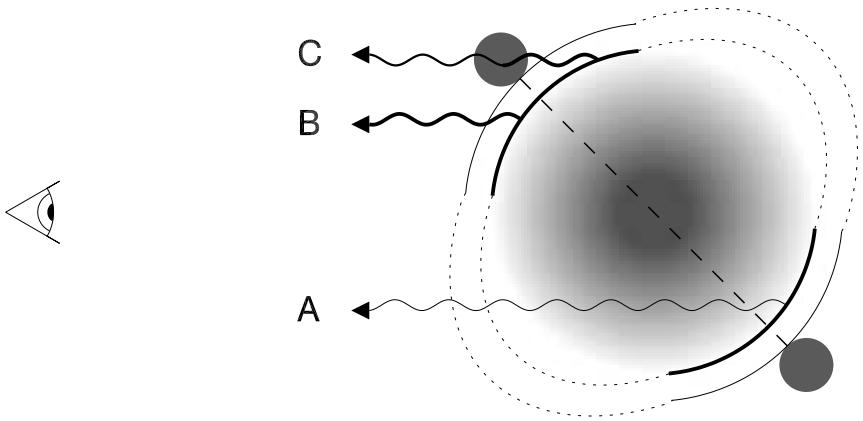

FIG. 16.—Diagram of a cross section of the remnant showing emission originating from different regions of the reverse shock. The dashed line shows the equatorial plane, which is inclined at ~44° to our line of sight (*the direction of which is shown by the eye*). The two shaded circles represent the cross section of the equatorial ring. Arcs about the equator show the locations of the reverse shock (*thick lines*) and the blast wave (*thin lines*). The dotted lines show hypothetical locations of these shock fronts in the polar regions. The inner gray-scale gradient represents the density of the SN debris, which decreases with radius. Emission from the reverse shock (*wavy arrows*) along the line of sight labeled A comes from the far side of the remnant and may suffer extinction by dust in the debris. Because of resonant scattering (§ 5.3), the Lyα emission arriving from the far side of the remnant is diminished. The Lyα emission along line of sight B is augmented by the resonant scattering process. Reverse-shock emission from the near side of the remnant along line of sight C, which lies behind the equatorial ring is subject to extinction by dust contained by the gas in the ring.

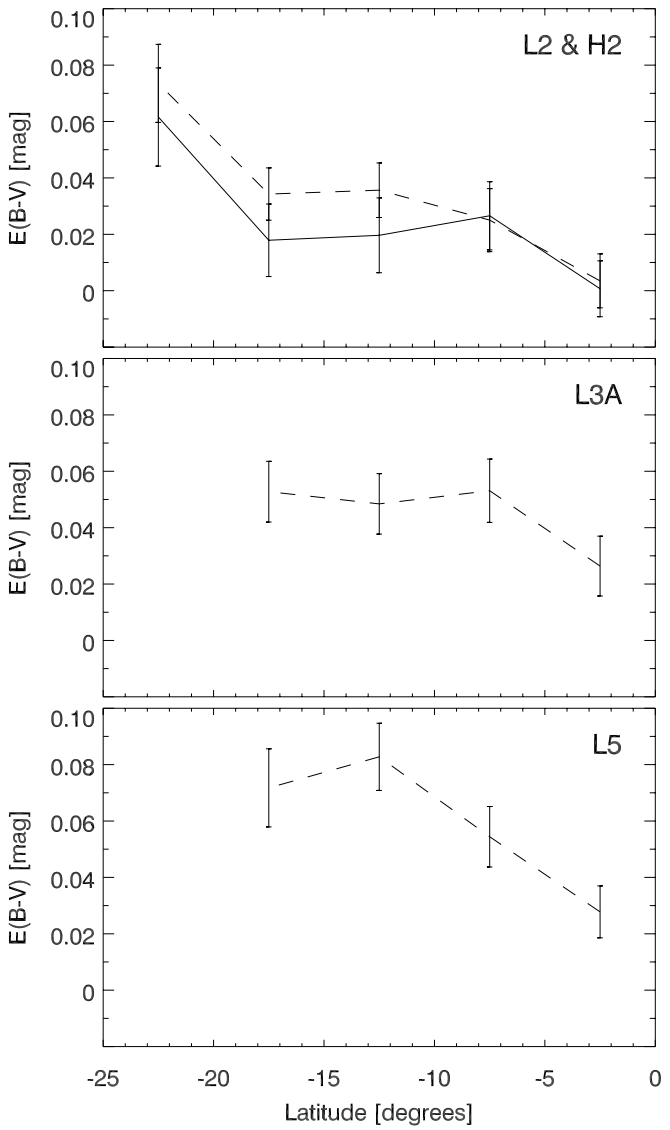

FIG. 17.—Extinction caused by the equatorial ring. For epoch 2, the solid line shows the reddening values obtained from the observed behavior of the Hα/Lyα ratio as a function of latitude. The dashed lines show the amount of extinction required assuming that the Lyα emissivity of reverse shock at negative latitudes equals that measured for 0°–20° latitude.

substantially fainter than that from the near side in Hα (by factors of $\sim$0.7) and much fainter in Lyα (by factors of $\sim$0.2). Clearly, the faintness of the reverse shock on the far side cannot be explained by the hypothesis that the mass flux through the reverse shock is much less there, because the observed ratio Hα/Lyα is much greater for the emission on the far side.

It is tempting at first glance to attribute the faintness of the reverse shock emission on the far side of the remnant to extinction by dust within the supernova debris, in the same way that we have accounted for the Hα/Lyα ratios observed on the near side. Such an interpretation would require that the debris contributes $E(B-V)_{\rm debris} \approx 0.14$ mag for the two lines of sight through the interior sampled by the epoch 2 and 3 observations. The model is physically unlikely, however. If the outer supernova debris has LMC abundances, and if all the refractory elements there have turned to dust, we could only account for a value $E(B-V)_{\rm debris} \lesssim 0.001$ mag. One might hypothesize that the supernova explosion injected newly synthesized refractory elements such as Si into the outer debris. If so, the Si-enriched gas would have to extend to radial expansion velocities $V \approx 10,000$ km s^{-1} in order for the line of sight to the far side of the debris to intercept the resulting dust. The spectrum of the SN at the time that the photosphere had this radial velocity showed no evidence of such enrichment. We did see evidence that clumps of newly synthesized ^{56}Co extend to radial velocities $V \approx 6000$ km s^{-1}, so we cannot rule out the possibility that clumps of newly synthesized Si extend to greater velocities. But we doubt it.

5.3. Lyα *Resonant Scattering*

Instead, we favor another interpretation. Lyα photons, unlike Hα photons, have a high probability of resonant scattering in the (mostly H II) outer supernova debris. The Sobolev optical depth for resonant scattering of a Lyα photon is $\tau_s \approx 1000$ at the location of the reverse shock. Thus, a Lyα photon emitted at line center (relative to the nearby supernova debris) at the reverse shock has a very high probability of resonant scattering before it penetrates far into the debris. As the photon propagates into the debris, it will be redshifted relative to resonance in the local debris. Therefore, a photon emitted sufficiently far in the red wing of the line profile has a chance of propagating freely through the debris. However, a photon emitted in the blue wing of the line profile will redshift toward line center as it propagates into the debris and will have an increased probability of resonant scattering.

Most Lyα photons emitted at the reverse shock will scatter many times before they emerge from the debris. At each scattering, the probability that the photon will escape in the outward direction is greater than the probability that the photon will escape by propagating inward through the entire SN envelope. Therefore, Lyα photons emitted by the reverse shock will escape preferentially from the side of the remnant from which they were produced.

We have carried out Monte Carlo simulations of this phenomenon with a simplified one-dimensional (two-stream) scattering model to see whether it might account for the asymmetry seen in the Lyα line profiles. In the comoving reference frame of the freely expanding supernova debris all H II atoms in the debris absorb Lyα at a centroid wavelength of 1215.67 Å. Photons are redshifted according to $z = l/ct_{\rm obs}$, where l is the distance traveled and $t_{\rm obs}$ is the time since the supernova explosion. Lyα photons escape from the remnant by diffusing both spatially and spectrally.

In our simulation photons are created at random locations in the ionization zone (with thickness $\sim 10^{14}$ cm) behind the reverse shock (located at $R = 4.5 \times 10^{17}$ cm). They are produced with a Voigt profile with narrow thermal width. We assign random directions (either inward or outward) to the photons and then calculate the optical depth for each photon along its path, taking into account the photon's redshift as it travels through the debris. Unless a photon is created or scattered very close to the reverse shock front or has a wavelength sufficiently far in the red wing of the absorption profile, it will be scattered somewhere in the debris. We determine the scattering location by assuming that the probability for absorption is proportional to $e^{-\tau(l)}$, where $\tau(l)$ is the optical depth along the photon's path.

We assume that the wavelengths of the scattered photons are determined by Hummer's type II redistribution function (Hummer 1962). With this redistribution function a photon will on average diffuse a thermal width from the wavelength at which it was absorbed. After selecting a new propagation direction for the scattered photon, we calculate the optical depth along its new path to determine where it will scatter next or whether it will escape from the remnant. When the photon eventually escapes the remnant we record the direction in which it escapes (from either the side of the remnant where it was initially emitted or from the other side) and calculate its observed wavelength. For our simulations we have assumed that the debris has uniform density throughout and that there is no means for destruction of photons (i.e., there is no dust or molecular lines that can absorb the photons).

Our simulations confirm our expectation about the asymmetry of emission escaping from the reverse shock. If the shock surface has intrinsic emissivity ϵ, half of which is emitted initially in the outward direction and half of which is emitted inward, the emergent photon flux can be written as $\epsilon/2(1+\alpha)$ in the outward direction and $\epsilon/2(1-\alpha)$ in the inward direction. Our simulations yield a value for the asymmetry parameter of $\alpha \approx 0.6$.

In addition to introducing an asymmetry in the emergent flux, the scattering process also affects the shape of the emergent line profile. Photons scattering through the remnant will be redshifted from their initial wavelengths, producing a red wing to the line profile (see § 6).

Our one-dimensional radiative transfer model is too simplified to give us an accurate quantitative estimate of α for the problem at hand. Nevertheless, it does give us confidence that resonance scattering can cause substantial asymmetry in the emission. Since a detailed three-dimensional calculation is beyond the scope of this paper, we take the value of α as a free parameter.

Figure 18 plots, as a function of the asymmetry parameter, α, the contribution of extinction by dust to the remnant and within the remnant required to fit the epoch 2 and 3 observations. In order that the extinction by dust within the debris have a reasonable value [$E(B-V)_{\rm debris} \lesssim 0.001$ mag], we require that $\alpha \sim 0.6$ to make the intrinsic Hα/Lyα emissivity ratios equal to 0.21 on both the near and far sides of the remnant. This value of α is coincidentally similar to that obtained from our simple scattering simulation. Since the assumed asymmetry parameter also enhances the brightness of Lyα on the near side of the remnant, the fit will require us to infer a value for the interstellar contribution of dust, $E(B-V) = 0.17 \pm 0.01$ mag, which is greater than the value we inferred previously and agrees well with measurements of the interstellar extinction to nearby stars.

5.4. *Reverse-Shock Emission Light Curve*

Our determination of the reverse shock expansion velocity obtained in § 5.1.1 was derived solely from astrometry of the reverse-shock's location. Here we determine the expansion velocity from the rate of brightening of the reverse-shock surface. This independent determination is, however, sensitive to the assumed properties of a specific hydrodynamic model for the expanding remnant. Here we consider a simplified model in which the reverse shock expands with constant velocity and the SN debris has a power-law density profile.

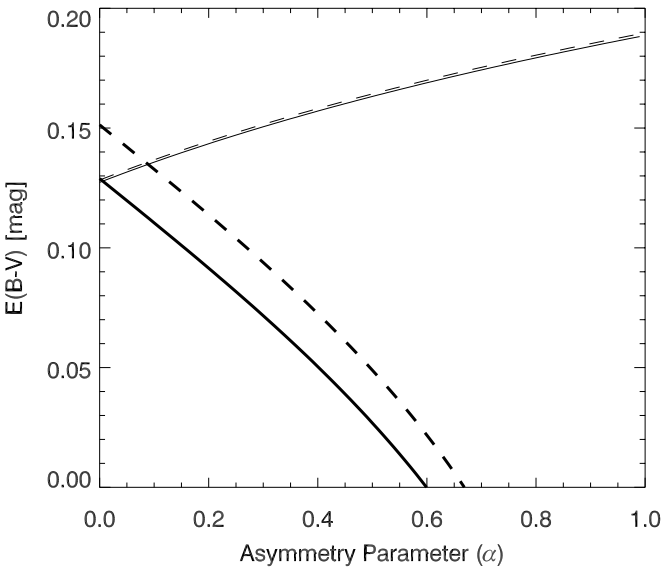

FIG. 18.—Contributions of extinction by dust as a function of the asymmetry parameter (α) due to Lyα scattering in the envelope. Thin lines show the amount of interstellar dust extinction, while thick lines show the amount of dust in the line of sight through the debris. These curves are calculated by requiring that the Hα/Lyα ratios observed in epochs 2 (*solid lines*) and 3 (*dashed lines*) match the intrinsic ratio calculated in § 3.

The emissivity of the reverse-shock surface is proportional to the mass flux per unit area crossing it,

$$\dot{m} = \rho(r_{\rm rs}, t_{\rm obs})(v_{\rm debris} - v_{\rm rss}) \ ,$$

where $\rho(r_{\rm rs}, t_{\rm obs})$ is the density of the envelope at the reverse shock at time $t_{\rm obs}$, $v_{\rm debris} = r_{\rm rs}/t_{\rm obs}$ is the velocity of the freely expanding debris at the reverse shock, and $v_{\rm rss}$ is the outward velocity of the reverse-shock surface. We assume that the density profile in the outer envelope is represented by a power-law profile,

$$\rho(r,t) = At^{-3}\left(\frac{r}{t}\right)^{-n} \ ,$$

where A is a normalization factor. Letting $\delta = v_{\rm rss}/v_{\rm debris}$, the emissivity of the reverse-shock surface can be written

$$\epsilon_{\rm rs} = \frac{\eta A}{\mu_p} t_{\rm obs}^{(n-4)} r_{\rm rs}^{(1-n)}(1-\delta) \ ,$$

where η is the production efficiency of Lyα or Hα per hydrogen atom crossing the shock front and μ_p is the mean mass per hydrogen atom in the envelope. With this relation, we can use the observed light curve to measure $v_{\rm rss}$ independently of our results in § 5.1.1 and to constrain the values of n and the normalization factor of the envelope density profile (ρ_0, the density at $t = 10$ yr and $v = 10^4$ km s^{-1}).

Figure 19 plots the light curve of the reverse shock in the northeast equatorial region of the remnant. We concentrate on the northeast quadrant since emission from the near side of the remnant is not subject to variable extinction by the debris. To compare the observed Lyα and Hα emissivities (tabulated in Table 4), we correct them for differential extinction by interstellar dust with $E(B-V) = 0.17$ mag and scale them by their production efficiencies. The Lyα emissivities have been reduced by an additional factor of 1.6 to account for the asymmetric emission of Lyα caused by resonant scattering as discussed in § 5.3.

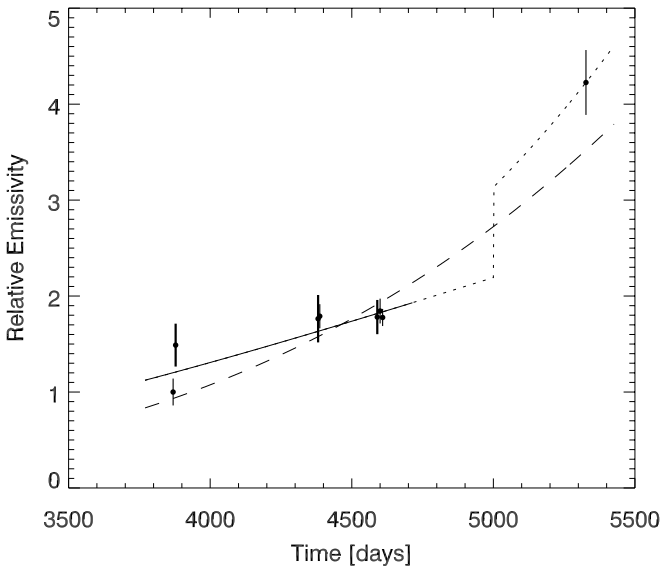

FIG. 19.—Surface emissivity of the reverse shock in the northeast equatorial regions of the remnant as a function of time. Thin error bars show Lyα emissivities, and thick error bars show Hα emissivities scaled to Lyα assuming Hα/Lyα = 0.21, $E(B-V) = 0.17$ mag, and $\alpha = 0.6$. Also shown are fits to the light curve assuming a constant rate of expansion for all epochs (*dashed curve*), a constant expansion for early epochs (*solid line*), and a model in which the reverse shock decelerates at day 5000 (*dotted line*).

Taking $\eta_{\mathrm{Ly}\alpha} = 1$ and $\mu_p = 2$ amu, we find the normalization of the SN envelope density for the equatorial northeast regions of the debris to be $\rho_0 = 450 \pm 80$ amu cm^{-3}, in agreement with the value predicted by Woosley (1988).

Figure 19 also displays some fits to the light curve. For these fits we have assumed $r_{\mathrm{rs}} = 4.6 \times 10^{17}$ cm at $t = 3869$ days (from the L1 observation), although our results are insensitive to this choice. Assuming $n = 9$, the fit to the entire light curve implies an upper limit to the expansion velocity of $v_{\mathrm{rss}} \lesssim 1000$ km s^{-1}. This value is much lower than the expansion rates of the radio ($v \approx 3500$ km s^{-1}; Manchester et al. 2002) and X-ray ($v = 5200 \pm 2100$ km s^{-1}; Park et al. 2002) images and the blast-wave velocity ($v = 3400 \pm 700$ km s^{-1}) inferred from the width of the X-ray line profile (Michael et al. 2002). We cannot remove this discrepancy by allowing n to vary.

The fit to the full light curve is not very good (reduced $\chi^2 = 2$), with the low expansion velocity being forced by the high emissivity of the L5 observation. It appears that the rate of increase of mass flux across the reverse shock in the northeast has accelerated. Moreover, the reverse-shock emission peak for that region seen in the L5 profile (Figs. 7 and 11) is much broader than those in previous observations and in our simulations. This suggests that the radius of the reverse shock varies by as much as $\sim$10% over regions of the surface contained by the slit.

It is possible that rapid brightening and distortion of the reverse shock is being caused by denser blobs in the supernova debris reaching the reverse shock. However, we expect that the reverse-shock front will be decelerated and distorted by the arrival of reflected shocks created when the blast wave struck the dense equatorial ring (Luo, McCray, & Slavin 1994; Borkowski et al. 1997b), and so we favor this explanation for the observed changes in emission from the reverse shock. We obtain better fits to the light curve if we assume that the reverse shock decelerated sometime between epochs 3 and 5 (i.e., between days 4600 and 5327). When we exclude the L5 observation from the fit (*solid line*) we infer $n = 9.0 \pm 0.5$ and an expansion rate of $v_{\mathrm{rss}} = 3700 \pm 900$ km s^{-1}, consistent with other observations. Depending on when (and if) the expansion decelerated, we find that v_{rss} can have a value between -500 and 1000 km s^{-1} at day 5327.

6. INTERIOR EMISSION

Up to now we have concentrated on the emission from the reverse shock. But, as the maps in Figures 7–10 show, we also detect Hα and Lyα emission from the interior of the remnant. Moreover, the Hα and Lyα emission from the interior have quite different distributions. Here we consider possible sources of this interior emission.

Since the envelope is optically thin to Hα, it is safe to assume that the Hα emission maps trace the local production of Hα photons. The Hα emission from the interior is centrally concentrated, falling off nearly exponentially with radius, and constant in time (within measurement errors). We expect that most of this emission is caused by late-time radioactive decay of ^{44}Ti, which has a half-life of $\sim$85 yr. Although the gamma rays produced in this decay easily escape the remnant, the energetic positrons from this reaction will deposit their energy locally. Using the expression for the energy input from positrons from the decay of ^{44}Ti given by Kozma & Fransson (1998), and assuming that Hα is produced with an efficiency of 1% (Xu & McCray 1991), we estimate that the Hα luminosity of the inner debris should be of order $L_{\mathrm{H}\alpha} \approx 10^{34}$ ergs s^{-1}. Correcting the H3 observation for interstellar extinction and extrapolating to the full volume of the debris, we estimate (roughly, say, within a factor of 2), the total Hα luminosity of the inner debris to be $L_{\mathrm{H}\alpha} \approx 10^{34}$ ergs s^{-1}, which supports our expectation.

The interior glow in the Lyα profiles is very different from the Hα interior emission (see, e.g., Fig. 10). It is more uniform than in Hα and is not centrally concentrated. This result is not surprising, considering that the supernova debris is much more opaque to Lyα photons than to Hα because of dust and resonant scattering. Both of these effects will suppress Lyα emission from the deep interior of the remnant. Assuming an efficiency of 35% for production of Lyα from the energy deposited by positrons (Xu & McCray 1991), we estimate a luminosity of $L_{\mathrm{Ly}\alpha} \approx 4 \times 10^{35}$ ergs s^{-1} for interior Lyα emission. The observed interior Lyα emission has an average volume emissivity $\epsilon_{\mathrm{Ly}\alpha} \approx 10^{-18}$ ergs s^{-1} cm^{-3} (corrected for interstellar extinction). If we assume that this emission uniformly fills the entire volume interior to the reverse shock, we estimate (again, with an uncertainty of roughly a factor of 2) a Lyα interior luminosity of $L_{\mathrm{Ly}\alpha} \approx 10^{36}$ ergs s^{-1}.

At first glance it may appear that radioactivity might account for this emission. We are doubtful, however. We expect that extinction by interior dust should greatly reduce the value of $L_{\mathrm{Ly}\alpha}$ that emerges from the remnant, especially since a Lyα photon must spatially diffuse from the interior through resonance scattering. This hypothesis is supported by the fact that, unlike the Hα interior emission, which is centrally concentrated, we see very little, if any, Lyα emerging from the center of the remnant. Moreover, we find that the interior Lyα emission, unlike the Hα emission, increases with time, contrary to the behavior expected from

radioactive decay. Therefore, we suspect that another source is responsible for most of the Lyα interior emission and that this source is related to the remnant's interaction with its environment.

What can this energy source be? An obvious suspect would be the X-ray emission originating from the blast wave. But the observed X-ray emission at present is too faint ($L_{\text{X-ray}}/L_{\text{Ly}\alpha} \approx 0.1$; Michael et al. 2002) to account for the observed Lyα emission. Another possible source is excitation by nonthermal particles that are produced by the remnant's shocks and diffuse into the debris. Indeed, plenty of energy is available, even assuming a very low efficiency of producing nonthermal particles in the shocks. However, if nonthermal particles were responsible for the Lyα emission, we would expect them to produce Hα with luminosity ratio $L_{\text{H}\alpha}/L_{\text{Ly}\alpha} \approx 0.04$, in conflict with the observed ratio $L_{\text{H}\alpha}/L_{\text{Ly}\alpha} < 0.01$.

The fact that the Lyα interior luminosity is comparable with the Lyα luminosity of the entire reverse shock ($L_{\text{Ly}\alpha}/L_{\text{rs}} \approx 0.5$) suggests that we consider the reverse shock itself as the main source of the interior Lyα photons. Indeed, the interior Lyα emission may result from the same resonance scattering process by which Lyα photons are reflected from the reverse shock (§ 5.3). In Figure 20 we plot the Lyα profile taken from one spatial location along the slit from the L3B observation. The interior emission falls off with increasing wavelength and extends to wavelengths greater than 1300 Å. Such high wavelengths would imply that these photons originate from behind the reverse shock on the far side of the remnant, which is physically unreasonable. However, when scattering in the Lyα line is considered, we find that the Doppler shift of a Lyα photon from the "interior" region of the line profile may not correspond to the position along the line of sight from which it last scattered.

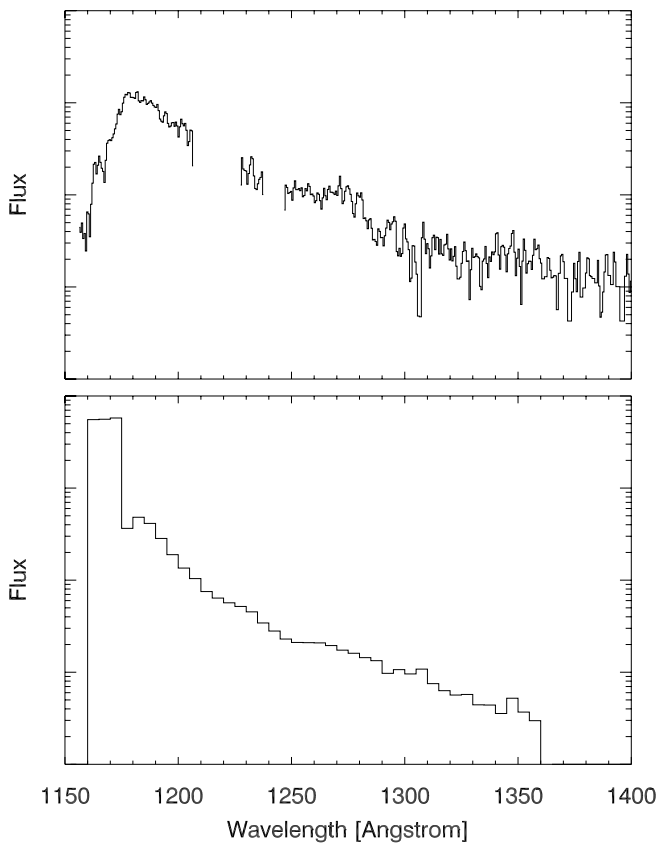

FIG. 20.—Lyα "interior" emission profiles. *Top:* The observed profile from one spatial region of the L3B observation. Blank regions are due to the contaminants discussed in § 2.1. *Bottom:* The Lyα profile produced by our one-dimensional Monte Carlo simulation of resonant scattering in the Lyα line. Although photons in this profile are originally produced on the near side of the remnant, they can emerge from the remnant substantially redshifted.

Photons that are originally produced at the reverse shock on the near side of the remnant can diffuse to wavelengths slightly longer than the local Lyα resonant wavelength via multiple scattering. Once redward of the line core, photons can traverse large distances without being absorbed. Of the photons traveling inward, many will simply escape out of the far side of the remnant. However, some may be scattered once more in the wing of the Lyα line. If these photons are back-scattered they will be redshifted farther and can easily escape through the near side of the remnant. Such photons can then have redshifted velocities as high as $v = 3R_{\text{rs}}/T_{\text{obs}}$ (3 times that observed from photons directly coming from the reverse shock surface). We see this effect in our simple one-dimensional Monte Carlo scattering simulation (§ 5.3). Figure 20 also plots a simulated Lyα line profile resulting from the scattering of photons produced at the reverse shock surface. Without scattering, the photons would all emerge with the same wavelength ($\lambda = 1170$ Å). While our simplified simulation is inadequate to model the observations quantitatively, the fact that Lyα photons are distributed redward of the reverse shock emission (even to wavelengths greater than 1300 Å) is encouraging.

There exists another interesting effect caused by Lyα resonant scattering. N v $\lambda\lambda$1239, 1243 photons produced by the brightening spots on the ring that travel into the SN envelope will appear blueshifted to the oncoming gas. For each point of origin of N v $\lambda\lambda$1239, 1243 photons (such as a spot on the ring) there is a surface in the interior debris (Fig. 21) on which the N v $\lambda\lambda$1239, 1243 photons will be blueshifted into resonance with Lyα. When N v $\lambda\lambda$1239, 1243 photons reach this surface they will be trapped and will have to escape from the remnant through the same scattering process as Lyα photons produced at the reverse shock. How these surfaces will appear in the Lyα line profile will depend on the how these photons escape from the interior of the remnant through multiple scattering. At present the luminosity of N v $\lambda\lambda$1239, 1243 from the remnant is too faint ($L_{\text{NV}} \lesssim 10^{35}$ ergs s^{-1}) to see signatures of this effect. However, as the N v $\lambda\lambda$1239, 1243 emission from the spots on the ring increases (perhaps by a factor of 10 within a few years), these resonant scattering surfaces will brighten and begin to contribute significantly to the interior component of the Lyα line profile.

7. DISCUSSION

We have shown that resonant scattering in the Lyα line is an important process through which these photons escape from the remnant (§ 5.3). A full three-dimensional simulation of resonant scattering in the Lyα line is warranted since the asymmetry parameter α most likely depends on the viewing angle of the reverse-shock surface. The value of this parameter will affect our determination of the extinction in front of and within the remnant. We note, however, that although our one-dimensional scattering simulation does produce a red wing to the Lyα line, the overall reverse-shock

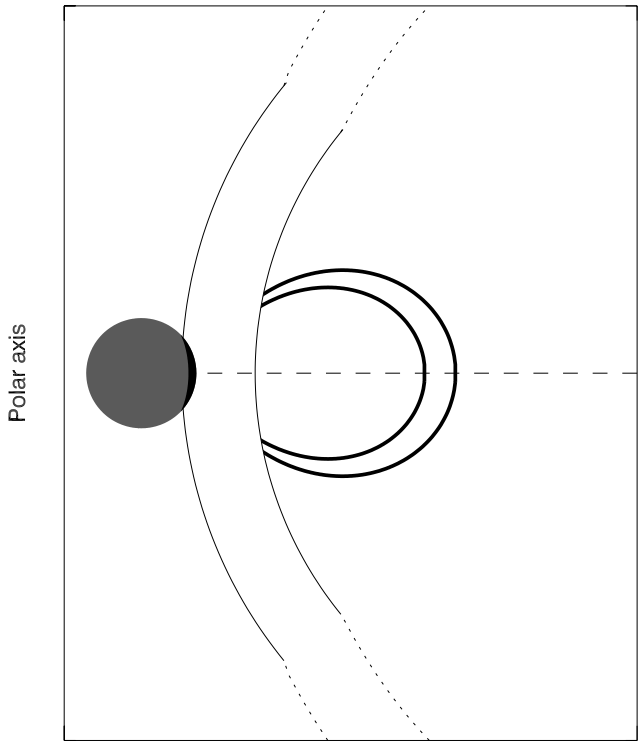

FIG. 21.—Diagram of a cross section of the remnant demonstrating the surfaces in the SN envelope where N v $\lambda\lambda$1239, 1243 emission from a spot (*dark crescent*) on the ring (*shaded circle*) will be resonantly scattered in the Lyα line of hydrogen. The dashed line shows the location of the equatorial plane. Arcs about the equator show the locations of the reverse shock and blast wave, with dotted lines showing the hypothetical location of these shock fronts in the remnant's polar regions. The two thick curves show the resonant scattering surfaces for each component of the N v $\lambda\lambda$1239, 1243 doublet originating from the spot.

emission peak in the line profile is not affected at the spectral resolution of our present observations. Therefore we are confident that the scattering process has not affected our measurements of the reverse-shock geometry.

Since the envelope is optically thin to Hα scattering, the observed difference in Hα emissivity on the near and far sides of the remnant represents a real asymmetry of $\sim$30% in the mass flux through the reverse shock. Some of this asymmetry ($\sim$20%) may be attributed to time-of-flight delays across the remnant. (We see the rapidly brightening reverse shock on the far side as it was $\sim$6 months earlier than the time at which we see the reverse shock on the near side.) Any additional asymmetry in the Hα brightness would then represent real asymmetry in the mass flux through the reverse shock in the near and far sides of the remnant. Besides a front/back brightness asymmetry, we also observe differences in brightness between other regions of the reverse shock. The reverse shock in the northeast quadrant is noticeably brighter than elsewhere. The appearance of asymmetries in the reverse shock is not a great surprise since other observations have shown the remnant to be asymmetric. Most of the bright spots on the equatorial ring appeared first in the east, and both radio (Manchester et al. 2002) and X-ray (Park et al. 2002; Michael et al. 2002) images are $\sim$50% brighter on that side of the remnant. The observed Hα emission seems to correlate with this east-west asymmetry; from the H4N and H4S observation we measure that the reverse shock in the east is $40\% \pm 20\%$ brighter than it is in the west.

The reverse shock may be brighter in a given direction either because it is encountering denser circumstellar gas in that direction or because the supernova debris itself is denser in that direction. If the latter interpretation is correct, we would have the remarkable conclusion that the supernova debris lacks even cylindrical symmetry.

In principle, we should be able to distinguish between these possibilities from the location of the reverse shock. In the former case, the blast wave and the reverse shock will not propagate as far in the direction of the denser circumstellar gas, while in the latter case the shock will have propagated farther.

At first glance, we might prefer the latter interpretation because most of the brightening spots seen so far have appeared on the east side of the remnant, where the reverse shock and X-ray emission are brighter. However, our measurements of the reverse shock indicate that the blast wave is at a smaller radius in the east (relative to the supernova centroid). This result favors the former interpretation. If so, the spots appeared first in the east because inward protrusions of the dense circumstellar ring just happen to be in those directions. However, the astrometry that has been possible up to now is not accurate enough to settle the matter.

More observations will help resolve this issue, as well as other outstanding questions about emission from the reverse shock. As the emissivity of the reverse shock increases, we will be able to observe the high-velocity line profiles with narrower slits. With a 0.″05 slit we can dramatically increase the spatial resolution of the observations, enabling us to see finer scale structure in the shock front and to determine its location more precisely. Also, the line profiles obtained through a narrow slit will be less contaminated, allowing us to measure emission from larger regions of the reverse shock.

Identical Hα and Lyα observations using a narrow (0.″05) slit aligned along the ring's minor axis would be ideal for measuring extinction by the debris and ring system. With such an alignment, emission from the reverse shock will be maximally blocked by the near portion of the ring. Also, the effect of the damped Lyα absorption will be minimized since the emission from the reverse shock in this orientation will have the maximum line-of-sight velocity.

To measure the position of the reverse shock more accurately, we must reduce the uncertainty in the registration of the SN centroid in the spectra. For the present Lyα profiles we have been forced to use emission from spot 1 (and in worse cases, diffuse emission from the ring) to measure the position of the reverse shock. This is not ideal since the spots have proper motions (Sugerman et al. 2002). Also, as the spots become resolved we will have to contend with the fact that their UV and optical emission may come from spatially distinct regions (Pun et al. 2002).

Ideally we would use stars to register the location of the SN. However, since there are few UV stars in the surrounding field, it is difficult to orient the slit so that it contains a star. Therefore, we recommend an alternative observational approach. First, acquire and center a nearby UV star (e.g., star 2) in the desired slit. Measure a spectrum of this star with the G140L grating in place. Then slew the telescope to the desired slit position on the remnant and measure another spectrum. Since *HST* can perform small offsets very precisely, we can use the location of the star in the first

spectrum to register the SN location in the second spectrum. With this procedure, we can avoid the nonrepeatability of the optical path introduced by the mode select mechanism that has confounded our previous astrometry.

Continued observations of emission from the reverse shock will allow us to monitor the rapid changes in its geometry, expansion rate, and luminosity. Since most of the remnant's mass is still in the expanding SN debris and not in the swept-up shell, the expansion of the remnant is driven by the material crossing the reverse shock. By comparing observations of the development of the reverse shock with those of the X-ray emission from the blast wave and the brightening spots on the equatorial ring, we have a unique opportunity to develop a full picture of the global hydrodynamics of the birth of this remarkable supernova remnant.

E. M. would like to thank Svetozar Zhekov for many useful conversations over the years and John Blondin for his expertise and help with the hydrodynamic simulation code VH-1. This research was supported by NASA through grants NAG 5-3313 and NTG 5-80 to the University of Colorado, and through grants GO-8243, GO-8648, and GO-9114 from the Space Telescope Science Institute, which is operated by the Association of Universities for Research in Astronomy, Inc., under NASA contract NAS 5-26555.

REFERENCES

Blondin, J. M., Lundqvist, P., & Chevalier, R. A. 1996, ApJ, 472, 257
Borkowski, K., Blondin, J., & McCray, R. 1997a, ApJ, 476, L31
———. 1997b, ApJ, 477, 281
Burrows, C. J., et al. 1995, ApJ, 452, 680
Burrows, D. N., Michael, E., Hwang, U., McCray, R., Chevalier, R. A., Petre, R., Garmire, G. P., Holt, S. S., & Nousek, J. A. 2000, ApJ, 543, L149
Cargill, P. J., & Papadopoulos, K. 1988, ApJ, 329, L29
Chevalier, R. A. 1982, ApJ, 258, 790
Chevalier, R. A., Kirshner, R. P., & Raymond, J. C. 1980, ApJ, 235, 186
Crotts, A. P. S., Kunkel, W. E., & Heathcote, S. R. 1995, ApJ, 438, 724
Eastman, R. G., & Kirshner, R. P. 1989, ApJ, 347, 771
Fitzpatrick, E. L. 1986, AJ, 92, 1068
———. 1999, PASP, 111, 63
Fitzpatrick, E. L., & Walborn, N. R. 1990, AJ, 99, 1483
Ghavamian, P., Raymond, J., Smith, R. C., & Hartigan, P. 2001, ApJ, 547, 995
Hummer, D. G. 1962, MNRAS, 125, 21
Janev, R. K., & Drawin, H. W. 1993, Atomic and Plasma-material Interaction Processes in Controlled Nuclear Fusion (New York: Elsevier), 373
Kozma, C., & Fransson, C. 1998, ApJ, 496, 946
Lawrence, S. S., Sugerman, B. E., Bouchet, P., Crotts, A. P. S., Uglesich, R., & Heathcote, S. 2000a, ApJ, 537, L123
Lundqvist, P., & Fransson, C. 1996, ApJ, 464, 924
Luo, D., McCray, R., & Slavin, J. 1994, ApJ, 430, 264
Manchester, R. N., Gaensler, B. M., Wheaton, V. C., Staveley-Smith, L., Tzioumis, A. K., Bizunok, N. S., Kesteven, M. J., & Reynolds, J. E. 2002, Publ. Astron. Soc. Australia, 19, 207
Meaburn, J., Bryce, M., & Holloway, A. J. 1995, A&A, 299, L1
Michael, E., McCray, R., Borkowski, K. J., Pun, C. S. J., & Sonneborn, G. 1998a, ApJ, 492, L143
Michael, E., Zhekov, S., McCray, R., Hwang, U., Burrows, D. N., Park, S., Garmire, G. P., Holt, S. S., & Hasinger, G. 2002, ApJ, 574, 166
Michael, E., et al. 1998b, ApJ, 509, L117
———. 2000, ApJ, 542, L53
Nussbaumer, H., & Schmutz, W. 1984, A&A, 138, 495
Park, S., Burrows, D. N., Garmire, G. P., Nousek, J. A., McCray, R., Michael, E., & Zhekov, S. 2002, ApJ, 567, 314
Pengelly, R. M., & Seaton, M. J. 1964, MNRAS, 127, 165
Plait, P. C., Lundqvist, P., Chevalier, R. A., & Kirshner, R. P. 1995, ApJ, 439, 730
Pun, C. S. J., et al. 2002, ApJ, 572, 906
Scuderi, S., Panagia, N., Gilmozzi, R., Challis, P. M., & Kirshner, R. P. 1996, ApJ, 465, 956
Shigeyama, T., & Nomoto, K. 1990, ApJ, 360, 242
Sonneborn, G., et al. 1998, ApJ, 492, L139
Sugerman, B. E. K., Lawrence, S. S., Crotts, A. P. S., Bouchet, P., & Heathcote, S. R. 2002, ApJ, 572, 209
Wang, L., Wheeler, J. C., Kirshner, R. P., Challis, P. M., Filippenko, A. V., Fransson, C., Panagia, N., Phillips, M. M., & Suntzeff, N. 1996, ApJ, 466, 998
Wiese, W. L., Smith, M. W., & Glennon, B. M. 1966, in Atomic Transition Probabilities, Vol. 1 (NSRDS-NBS 4; Washington: GPO), 1
Woosley, S. E. 1988, ApJ, 330, 218
Xu, Y., & McCray, R. 1991, ApJ, 375, 190